6-26-2023

An Equivalent Point-Source Stochastic Model of the NGA-East Ground-Motion Models and a Seismological Method for Estimating the Long-Period Transition Period TL

Christine Assadollahi

AN EQUIVALENT POINT-SOURCE STOCHASTIC MODEL OF THE NGA-EAST GROUND-MOTION MODELS AND A SEISMOLOGICAL METHOD FOR ESTIMATING THE LONG-PERIOD TRANSITION PERIOD T_L

by

Christine Maurice Moore Assadollahi

A Dissertation

Submitted in Partial Fulfillment of the

Requirements for the Degree of

Doctor of Philosophy

Civil Engineering

The University of Memphis

August 2023

Acknowledgments

This document represents not only my work, but the talent, time, and efforts of several mentors. I want to acknowledge and thank the people who made a remarkable impact on my career and my life. First, I am grateful for my major advisor, Dr. Shahram Pezeshk, for his mentorship and guidance in completing this work, his support of my graduate school journey, and assistance starting my career in structural engineering. His strength, calm presence, and sincerity are all attributes I aspire to.

I would also like to express my gratitude for my committee members Dr. Charles Camp, Dr. Roger Meier, Dr. Mihalis Gkolias, and Dr. Farzad Naeim. Your contributions, comments, and advice greatly improved the quality of this document.

All my classmates and office mates made graduate school wonderful. There were long days and late nights, and they were always there to help me push through. I wish you all well in your endeavors.

I had the opportunity to work with many undergraduate students through my teaching assistantship assignments. I am grateful to each of you. Anytime you chose to seek my help in anything (preparing a report, studying for a test, applying for an internship), I was deeply honored.

Finally, I would like to thank all the faculty, staff, and students in the Herff College of Engineering at the University of Memphis collectively. You have left an indelible mark on my life.

Preface

This dissertation deals with the development of a ground-motion model for the Central and Eastern United States, and the calculation of the long-period transition period parameter, T_L. This dissertation is comprised of two related studies. The first study has been submitted for publication in the Earthquake Spectra journal, entitled "An Equivalent Point-Source Stochastic Model of the NGA-East Ground-Motion Models", and this study is discussed in Chapter 2 of this document. The second study is published in the Earthquake Spectra journal, entitled "A Seismological Method for Estimating the Long-Period Transition Period T_L in the Seismic Building Code", and this study is discussed in Chapter 3 of this document.

Abstract

This dissertation deals with the stochastic simulation of the Next Generation Attenuation-East (NGA-East) ground-motion models and a proposing a new method of calculating the long-period transition period parameter, T_L, in the seismic building codes. The work of this dissertation is carried out in two related studies. In the first study, a set of correlated and consistent seismological parameters are estimated in the in Central and Eastern United States (CEUS) by inverting the median 5%-damped spectral acceleration (PSA) predicted from the Next Generation Attenuation-East (NGA-East) ground-motion models (GMMs). These seismological parameters together form a point-source stochastic GMM. Magnitude-specific inversions are performed for moment magnitude ranges M_w 4.0-8.0, rupture distances R_{rup} = 1-1000 km and periods T = 0.01-10s, and National Earthquake Hazard Reduction Program site class A conditions.

In the second study, the long-period transition period parameter T_L is investigated, and an alternate seismological approach is used to calculate it. The long-period transition period parameter is utilized in the determination of the design spectral acceleration of long-period structures. The estimation of T_L has remained unchanged since its original introduction FEMA 450-1/2003; The calculation is loosely based on a correlation between modal magnitude M_w and T_L that does not account for different seismological parameters in different regions of the country. This study will calculate T_L based on the definition of corner period, and will include two seismological parameters, the stress parameters $\Delta\sigma$ and crustal velocity in the source region β, in its estimation. The results yield a generally more conservative (or longer) estimation of T_L than the estimation that is currently used in engineering design standards.

Table of Contents

List of Tables

List of Figures

Chapter 1: Introduction

The first part of this dissertation deals with the stochastic simulation of the Next Generation Attenuation-East (NGA-East) GMMs that yields a set of seismological parameters for the CEUS. In the stochastic method, a ground-motion intensity measure (GMIM) obtained from either existing data or predicted from an existing ground-motion model (GMM) is inverted, and certain seismological parameters are selected as variables to be determined from the inversion of the GMIM. The GMIM selected could be peak ground acceleration (PGA), peak ground velocity (PGV), or several other types. In this study, the median 5%-damped pseudospectral acceleration (PSA) predicted from a weighted average of the 17 NGA-East GMMs is inverted using a particle swarm optimization (PSO) algorithm. The assumed model used in this study is a point-source model in which the GMIM is predicted from the following multiplicative, additive, or a mixture of multiplicative and additive terms: source term, path term, site term, and instrumentation term. The source term models the source characteristics of the earthquake, the path term accounts for how the waves decay with distance, the site term accounts for the effects of the soil on the amplification of seismic waves, and the instrumentation term converts the Fourier amplitude spectrum (FAS) produced by the previous terms to the appropriate GMIM to match the inverted GMIM. In each term, some seismological parameters will be assumed from previous literature while others will be treated as unknown variables. Each seismological parameter will have an upper and lower bound. The result from using the stochastic method is a set of seismological parameters that can be used together to with a stochastic point-source GMM. In this study, magnitude-specific inversions will be performed for moment magnitude ranges M_w 4.0-8.0, rupture distances R_{rup} = 1-1000 km and periods T = 0.01-10s, and National Earthquake Hazard Reduction Program site class A conditions.

The next part of this dissertation reevaluates the calculation of the long period transition period parameter, T_L. T_L was developed in the 2003 edition of the Federal Emergency Management Agency 450-1: National Earthquake Hazard Reduction Program (NEHRP) Recommended Provisions for Seismic Regulations for New Buildings and Other Structures Provisions (hereafter called "FEMA 450-1") to account for the decreasing spectral acceleration as the period increases in design response spectra. There are two main issues with the current estimation of T_L used in the U.S. model building code and design standards: 1) the disaggregation of the moment magnitude has been re-completed several times and at longer spectral periods, however T_L has not been re-calculated based on new disaggregation results and 2) there was one equation chosen to calculate T_L nationally, so it does not account for differing seismological parameters throughout different regions of the United States. In this study, we will investigate using moment magnitudes to calculate T_L that are disaggregated at different spectral periods. T_L is assumed to be the inverse of the corner frequency (or cut-off frequency); so, we will use the seismological definition of corner period together with estimates of seismological parameters in the CEUS, WUS, and Hawaii (HI) to develop three unique equations to calculate T_L based on the three regions. The two seismological parameters used in this study are the crustal velocity in the source region (hereafter called "source velocity") and the stress parameter. This study is the first to investigate T_L in the U.S. model building code and design standards since its introduction in 2003.

The two studies are primarily related through the resulting stress parameter from the first study is used in the calculation of T_L in the second study; the first study is in its first round of review in Earthquake Spectra, and the second study is published in Earthquake Spectra.

Chapter 2: An Equivalent Point-Source Stochastic Model of the NGA-East Ground-Motion Models

Abstract

The main objective of this study is to estimate seismological parameters in Central and Eastern United States (CEUS), including the geometrical spreading, anelastic attenuation, stress parameter, and site attenuation parameters. In this study, we use particle swarm optimization (PSO) to invert a weighted average of the median 5%-damped spectral acceleration (PSA) predicted from the Next Generation Attenuation-East (NGA-East) ground-motion models (GMMs) to develop a point-source stochastic GMM with a well-constrained set of ground-motion parameters. Magnitude-specific inversions are performed for moment magnitude ranges M_w 4.0-8.0, rupture distances R_{rup} = 1-1000 km and periods T = 0.01-10s, and National Earthquake Hazard Reduction Program site class A conditions.

The result of this study yields a single stochastic GMM that yields similar PSA values as the median NGA-East GMMs. The parameters derived from this study can be used for hybrid empirical method (HEM) applications. This study is the first to perform a formal inversion using the GMMs developed for the NGA-East project. The approach has been validated by using simulated small-to-moderate magnitude and large-magnitude data derived from the NGA-West2 GMMs (Zandieh et al., 2016, 2018; Pezeshk et al., 2015).

Introduction

The objective of this study is to estimate a set of seismological parameters in the CEUS using the stochastic method that minimizes the misfit between the stochastic model's predicted ground-motion intensity measure (GMIM) and the GMIM from the weighted average of the median Next Generation Attenuation-East (NGA-EAST) ground-motion models (GMMs). The seismological parameters estimated include constraints on the

geometrical spreading, anelastic attenuation, stress parameter, and site attenuation parameters. The stochastic method is an effective method for modeling ground-motions by incorporating what is known about the source, path, and site characteristics into a functional form, and then estimating correlated seismological parameters through the inversion of GMIMs. The GMIMs can either be obtained from actual recorded data or from existing GMMs. In this study, we invert horizontal GMIMs predicted from the empirical NGA-EASTGMMs to estimate a consistent and correlated set of seismological parameters to use with an equivalent point-source stochastic model.

In this study, we will use a Particle Swarm Optimization (PSO) algorithm to simulate the 5% damped pseudo-spectral acceleration (PSA) predicted from the median of the NGA-East GMMs. The simulation will be performed for individual magnitudes, or magnitude-specific, for moment magnitudes M_w ranging from 4.0-8.0 in increments of 0.5. Here we will give background on the applications of the stochastic method, NGA-East GMMs, and PSO.

Applications of the Stochastic Method

The stochastic point-source model is a method used to simulate GMIMs in regions where recorded strong ground motions are lacking (Boore, 2003). There are several applications of the stochastic method within earthquake engineering and seismology. Tavakoli and Pezeshk (2005) and Pezeshk et al. (2011,2015, 2018) used the stochastic method as part of the hybrid empirical method (HEM), introduced by Campbell (2003), to develop GMMs for the CEUS using the empirical ground-motion prediction equations for Western United States (WUS). The HEM is used to map empirical estimates of ground motion from a region where strong-motion recordings are numerous (the host region) to be suitable for a region with sparse strong-motion recordings (the target region).In the HEM, the

ratio of stochastic simulations for the target region to those for the host region is used to scale the empirical estimates of ground motion from the host region to the target region.

As part of the NGA-West2 project, Dabaghi and Der Kiureghian (2014) employed the stochastic method by simulating near-fault ground motions for applications in performance-based earthquake engineering (PBEE). They performed probabilistic seismic hazard analysis (PSHA) for a near-fault site, which is the first step of PBEE. Dabaghi and Der Kiureghian (2014) concluded that synthetic ground motions that include directivity effects should be used in the PSHA of near-fault structures, since there is a scarcity of near-fault ground motions containing directivity pulses. They also noted that spectral matching cannot be used to incorporate a pulse from near-fault effects if one is not captured in the original ground motion, further expressing the usefulness of stochastic models. The inversion approach utilized in this study has been validated by Zandieh et al. (2016, 2018).

Next Generation Attenuation-East Ground-Motion Models (NGA-East GMMs)

The GMIM inverted in this study is the PSA predicted from the median of the NGA-East GMMs. Goulet et al. (2015) developed the NGA-East GMMs, and Goulet et al. (2018) developed an accompanying ground motion characterization (GMC) tool. The GMC tool computes a weighted average of the median GMIMs from 17 GMMs. The GMC tool is valid for magnitudes $4 \leq M_w \leq 8.2$, periods of $0.1\text{s} \leq T \leq 10.0\text{s}$, and rupture distances $1\text{ km} \leq R_{rup} \leq 1{,}500\text{ km}$. The median GMIMs are computed for a National Earthquake Hazards Reduction Program (NEHRP) site class A, which means the timed average shear-wave velocity of the top 30 meters of soil, V_{s30} is approximately 3,000 m/s.

Figure 1 shows: (1) the magnitude-distance range of the NGA-East GMMs, (2) the magnitude-distance range considered in this study, and (3) all events recorded in the NGA-

East Database (Goulet et al., 2014). The scope of the model from this study is comparable to the scope of the NGA-East GMMs.

As can be observed from Figure 1, the data used to develop the NGA-East GMMs is skewed to the distance range of 100 km $\leq R \leq$ 2000 km and magnitude range of 2.0 $\leq M_w \leq$ 5.9. Since many of the existing GMMs used to develop the NGA-East GMMs had to be extrapolated for large distances and magnitudes, we decided to base our model on the NGA-East GMMs rather than the NGA-East Database. By basing the model on the NGA-East GMMs, we can estimate the PSA from earthquakes with a large range of magnitudes and distances. If the model were based on the NGA-East Database, then an extrapolation method would need to be employed to estimate the PSA of earthquakes with larger magnitudes and shorter distances.

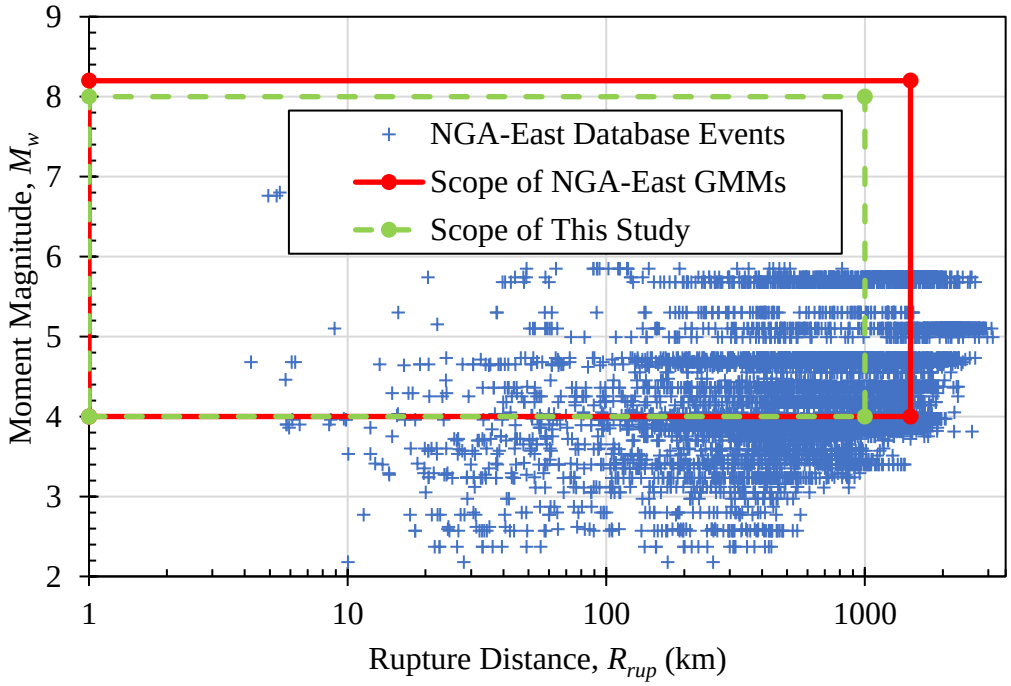

Figure 1. NGA-East Database Events and Scope of NGA-East GMMs Compared to Scope of This Study.

Particle Swarm Optimization (PSO)

In this study, we use PSO to perform the inversion. There are numerous methods to solve an inversion problem or complete a simulation. Metaheuristics are a popular class of algorithms used to solve non-linear inversion and non-linear combinatorial problems (Engelbrecht, 2007). Some metaheuristics include the genetic algorithm (GA), simulated annealing (SA), ant colony optimization (ACO), and PSO. Pace et al. (2021) reviewed the application of PSO in various geophysical inversion problems and provided practical guidance for solving an inversion problem using PSO; they also discussed the advantages and disadvantages of PSO and metaheuristics in general.

When there are many local optimal solutions (such as geophysical problems), initial solutions could lead to those local optima instead of the desired global optimal solution. Metaheuristics often have three components that help avoid a local optimal solution: (1) a random component, (2) search memory, and (3) a balance between the diversity of the search region and the intensity of searching a small region. These characteristics make metaheuristics a viable method of finding a high-quality solution, and each of the above components should be used when tuning hyperparameters for a metaheuristic.

PSO has been used in several applications related to seismology and geophysics. Lagos and Velis (2018) used PSO to detect and locate induced seismic events. Aleardi (2019) used PSO to solve two different non-linear geophysical optimization problems: seismic-petrophysical inversion and 1D elastic full-waveform inversion but noted that other metaheuristics could have been prime candidates to solve the problems given proper hyperparameter tuning. Song et al. (2012) applied PSO to the interpretation of Rayleigh wave dispersion curves to obtain shear-wave velocity profiles and recommended using PSO over GA or Monte Carlo (MC) approaches due to better reliability and faster computations.

Methodology

The objective of this study is to estimate a set of seismological parameters to develop a point-source stochastic model that minimizes the misfit between the model's predicted PSA and the PSA from the weighted average of the median NGA-East GMMs. The PSA is inverted, utilizing a PSO to yield a set of well-constrained, correlated seismological parameters.

Stochastic Method

We are using the stochastic method to develop a predictive model that relates the inputs of the earthquake moment magnitude M_w, rupture distance R_{rup}, and the structural frequency f, to the expected GMIM (in this study, PSA, hereafter called Y). The model is based primarily on the earthquake source, path, and site characteristics. From Boore (2003), Y is given by:

$$Y(M_0(M_w), R, f) = E(M_0(M_w), f)P(R, f)S(f)I(f) \quad (1)$$

where M_0 is the seismic moment, $E(M_0(M_w), f)$ is the source term, $P(R, f)$ is the path term, $S(f)$ is the site term, and $I(f)$ is the instrumentation term. Seismic moment is directly a function of the earthquake moment magnitude M_w and is defined by Hanks and Kanamori (1979) as:

$$M_0 = 10^{1.5(M_w+10.7)} \quad (2)$$

which yields the seismic moment in dyne-cm. We describe the main terms in the stochastic method here.

Source Term

The source term $E(M_0(M_w), f)$ is given by:

$$E(M_0(M_w), f) = \frac{10^{-20}\langle R_{\theta\Phi}\rangle FVM_0S(M_0,f)}{4\pi\rho_s\beta^3} \quad (3)$$

where $R_{\Theta\Phi}$ is the radiation pattern, F accounts for free-surface effects, V is the horizontal component of the total shear wave energy, $S(M_0, f)$ is the displacement source spectrum, ρ_s is the density of the of the crust in the source region, and β is the shear-wave velocity in the source region. The factor of 10^{-20} is included to account for ground motion expressed in cm, ρ_s expressed in gm/cc, and β is expressed in km/s. We use the recommended values by Boore (2003) and Kramer (1996) for $R_{\theta\Phi}$, F, and V. From Atkinson (2004), Boore et al. (2010), and Atkinson and Boore (2014), reasonable estimations of ρ_s and β are 2.8 g/cm^3 and 3.7 km/s, respectively.

The displacement source spectrum, $S(M_0, f)$, used in this study is the ω-squared model by Aki (1967), and used in Frankel et al. (1996), is given by:

$$S(M_0, f) = \frac{1}{1+\left(\frac{f}{f_c}\right)^2} \tag{4}$$

where f_c is the corner frequency. We used a single corner-frequency point-source spectrum in this study, defined by Brune (1970) as:

$$f_c = 4.9(10^6)\beta\left(\frac{\Delta\sigma}{M_0}\right)^{1/3} \tag{5}$$

where $\Delta\sigma$ is the stress parameter with units of bars. $\Delta\sigma$ is modeled as a function of magnitude in this study.

Path Term

The path term $P(R, f)$ is given by:

$$P(R, f) = Z(R)\exp\left(\frac{-\pi f R}{Q(f)\beta}\right) \tag{6}$$

where $Z(R)$ is the geometric attenuation or geometric spreading function, and $Q(f)$ is the anelastic attenuation function. $Z(R)$ and $Q(f)$ are highly correlated terms that both account for the decay of the amplitude of seismic waves due to different causes.

As waves propagate further away from the earthquake source, the area that the waves cover becomes larger, causing the waves' amplitude to decay, which is modeled using $Z(R)$. The geometric spreading function used in this study is a trilinear model given by Boore (2003):

$$Z(R) = \begin{cases} R^{b_1} & R \leq R_1 \\ {R_1}^{b_1}\left(\frac{R}{R_1}\right)^{b_2} & R_1 < R \leq R_2 \\ {R_1}^{b_1}\left(\frac{R_2}{R_1}\right)^{b_2}\left(\frac{R}{R_2}\right)^{b_3} & R > R_2 \end{cases} \quad (7)$$

where R_1 and R_2 are the hinge distances where the slope of the geometric spreading function changes, b_1, b_2, and b_3 are the slope of the $Z(R)$ for different ranges of R, and R is the effective point-source distance. For this study, R_1 was selected as 50 km and R_2 is 125 km to follow the same decay modeled by the path duration, which is mentioned below. In this study, b_1 and b_2 are determined as a function of magnitude from the inversion. Additionally, b_1 is modeled as frequency dependent. This is accomplished by inverting for b_1 at eight log-spaced frequencies between 0.1 Hz and 100 Hz and interpolating between the estimated values for all frequencies that are not at the eight log-spaced frequencies. Zandieh et al. (2018) first modeled a frequency dependent b_1 parameter in their stochastic simulation of the NGA-West GMPEs. The decay at longer distances is modeled by b_3, and has an estimated value of -0.5, which is used in this study (Atkinson, 2004; Boatwright and Seekins, 2011, Atkinson and Boore, 2014).

The method of interpolation for b_1 is a modified version of Akima's derivative formula, or Akima's spline (Akima, 1970). The MATLAB-specific modified version is called "Makima," which is the function name in MATLAB representing Akima's piecewise cubic Hermite interpolation method (Ionita, 2019). Akima's spline avoids excessive undulations, unlike other spline interpolation methods, but it can also recognize curves if there is a large

difference between successive data points. Akima's spline is a prime interpolation method for this application because the variation in b_1 goes from curved to flat rather quickly across frequencies (Zandieh et al., 2018).

R is sometimes used to account for the depth by incorporating a term referred to as the pseudo-depth term, effective depth term, or finite fault factor (Boore, 2003; Boore and Thompson, 2014). The effective point-source distance is modeled as:

$$R = \sqrt{{R_{rup}}^2 + h^2} \tag{8}$$

where R_{rup} is the rupture distance, and *h* is the finite fault factor determined from inversion. The authors wish to stress that referring to *h* as the "effective depth term" or the "pseudo-depth term" is a misnomer, as it is not supposed to be a term that indicates a physical depth value, but rather a term that accounts for near-source effects. In this study, *R* is modeled in the same manner in Boore et al. (1997).

The anelastic attenuation term is a different amplitude decay term used to account for decay due to the medium that the seismic waves propagate through. The anelastic attenuation term is modeled using:

$$Q(f) = Q_0 f^{\eta} \tag{9}$$

where Q_0 and η are parameters determined from the inversion.

Site Term

The site term *S*(*f*) is the product of the site amplification function *A*(*f*) and site-attenuation, or diminution, function *D*(*f*). The amplification function is dependent upon both the shear wave velocity of the soil and frequency. The diminution, or site-attenuation, function accounts for the high-frequency decay of the amplitude of the seismic waves, independent of the path term.

As mentioned before, the NGA-East GMMs yield median GMIMs for a NEHRP site class A (V_{s30} = 3000m/s). Inverting for the site amplification factors would result in too many parameters that are highly correlated with each other. So, we chose a generic site amplification function for the entire CEUS. Boore and Thompson (2015) developed crustal amplification factors for CEUS for the NEHRP Site Class A. Table 1 shows the crustal amplification factors used in this study from Boore and Thompson (2015).

Table 1. Site Amplification Factors (Table 5 of Boore and Thompson, 2015)

Frequency, *f* (Hz)	**Amplification, *A*(*f*)**
0.001	1.000
0.008	1.003
0.023	1.010
0.040	1.017
0.061	1.026
0.108	1.047
0.234	1.069
0.345	1.084
0.508	1.101
1.090	1.135
1.370	1.143
1.690	1.148
1.970	1.150
2.420	1.151

The diminution function $D(f)$ is defined as:

$$D(f) = \exp(-\pi\kappa_0 f) \tag{10}$$

where κ_0 is in units of seconds (Anderson and Hough, 1984). Typical values of κ_0 used in the CEUS vary from 0.002 s to 0.009 s, with a mean estimate of 0.006 s (Campbell et al., 2014). κ_0 is highly correlated with Q_0 and η (Anderson and Hough, 1984; Anderson, 1986; Anderson, 1991; Anderson et al., 1996). We determine Q_0 and η in this study; however, κ_0 was selected from previous studies. For this study, we used κ_0 = 0.006 s.

Instrumentation Term

The instrumentation term, $I(f)$, is a filter used to change from FAS to a different GMIM. In this study, the GMIM we need to compute is PSA. To convert the FAS to PSA, we used random vibration theory (RVT). Silva et al. (1997), Rathje and Ozbey (2006), and Rathje and Kottke (2008) used RVT for site response analysis. Kottke and Rathje (2008) generally described RVT in two main steps. First, conversion between time and frequency domain is completed using the Parseval's theorem. Then, the estimation of the peak factor is computed using extreme value statistics. Kottke and Rathje (2008) developed a point-source stochastic simulation program called STRATA. We used a similar RVT approach to STRATA in this study.

RVT requires two inputs: the FAS and the ground-motion duration (or the path duration), T_p. Table 2 summarizes the path duration model used in this study, in which we followed Boore and Thompson (2015).

Table 2. Path Duration Model (Table 3 in Boore and Thompson, 2015)

Point-Source Distance, R (km)	**Path Duration, T_p (sec)**
0	0.0
15	2.6
35	17.5
50	25.1
125	25.1
200	28.5
392	46.0
600	69.1
Slope of last segment	0.111

Table 3 summarizes the parameters that are determined from inversion (written in red), as well as selected parameter values with citations. We determine 13 parameters from the inversion.

Table 3. Summary of Model Parameters

Source, Path, Site, or Instrumentation	Stochastic Model Term; Relevant Equation	Parameter Value or Variable	Assumed from Literature or Estimated from Inversion
Source	Source Density, ρ_s; Equation 3	ρ_s = 2.8 g/cm^3	Atkinson and Boore (2014)
	Source Velocity, β; Equation 5	β = 3.7 km/s	Atkinson and Boore (2014)
	Stress Parameter, $\Delta\sigma$; Equation 5	$\Delta\sigma$	Inversion
Path	Geometric Attenuation, $Z(R)$; Equation 7	R_1 = 50 km, R_2 = 125 km, b_3 = -0.5	Boore (2003); Boore and Thompson (2015); Atkinson and Boore (2014)
		*b_1 and b_2	Inversion
	Finite Fault Factor, h; Equation 8	h	Inversion
	Quality Function, $Q(f)$; Equation 9	Q_0 and η	Inversion
Site	Site Amplification, $A(f)$	Table 1	Boore and Thompson (2015)
	Site-Attenuation, $D(f)$; Equation 10	κ_0 = 0.006 s	Campbell et al. (2014)
Instrumentation	Path Duration, T_p	Table 2	Boore and Thompson (2015)

*b_1 is technically 8 separate parameters determined in the inversion, as estimates are made at 8 log-spaced frequencies

Upper and Lower Bounds of Model Parameters

Choosing reasonable upper and lower bounds and truncating parameter values are methods used to reduce the search space and are important in accounting for trade-off between parameters. So, the estimation of one parameter effects the estimation of another. One such example of this is the correlation between the stress parameter and attenuation function. Boore (2015) studied the trade-offs between attenuation functions and the stress parameter as part of the NGA-East project by inverting eight earthquakes in Eastern North America (ENA) for a stress parameter with six different assumed attenuation models. Boore

(2015) also noted that including longer distances ($R_{rup} \leq 600$ km instead of $R_{rup} \leq 200$ km) resulted in lower stress parameters for all six attenuation models. For the case with R_{rup} constrained to lower than 600 km, the geometric mean of the stress parameter varied from 81 bars up to 961 bars, showing a large dependence upon the assumed attenuation functions. Since both attenuation function parameters and the stress parameter were estimated in this study, we applied reasonable upper and lower bounds on the search space of each parameter and allowed for the PSO algorithm to compare many solutions. The upper and lower bounds of each parameter were informed from previous studies. Table 4 summarizes the upper and lower bounds of each parameter in the inversion, applied truncating, and cites some of the research used to help determine reasonable upper and lower bounds.

Table 4. Model Parameter Bounds

Parameter	Bounds	Truncating	Literature Used to Determine Upper and Lower Bounds
$\Delta\sigma$	10 to 600 bars	Nearest 5 bars*	Boore (2012); Boore (2015); Atkinson (1993)
b_1	-1.3 to -0.6	Nearest 0.01	Boore (2015); Atkinson and Boore (2014); Yenier and Atkinson (2015)
b_2	-1 and 0.5	Nearest 0.01	
h	0 to 30 km	Nearest 0.1 km	Yenier and Atkinson (2014)
Q_0	250 and 800	Nearest 10	Atkinson and Boore (2014); Boatwright and Seekins (2011)
η	0.35 to 0.75	Nearest 0.01	

*This value was rounded

Particle Swarm Optimization (PSO)

The objective function that is to be minimized is given by:

$$Objective\ Function = \sqrt{\sum_{i,j} \left(\log(S_{i,j}) - \log(G_{i,j})\right)^2} \quad (11)$$

where $S_{i,j}$ is the stochastically predicted value of PSA from the inversions for distance i, spectral period j, and $G_{i,j}$ is the observed PSA. The objective function in Equation 11 is minimized separately for each magnitude, such that each magnitude is a separate inversion problem where the results from each inversion are aggregated (Zandieh et al., 2018). It

should be noted that a minimum value of the objective function is only one indicator of success of the model, so each result should be visually inspected as well.

Hyperparameter Tuning

The success of a metaheuristic algorithm in solving a problem, particularly a complex or highly dimensional problem, is dependent upon the parameters and hyperparameters chosen (Mostapha, 2016). the main parameters in a PSO algorithm are the swarm size n_s and number of iterations n_i, and the main hyperparameters are the inertia weight ω, the personal acceleration factor c_p, global acceleration factor c_g, and the inertial damping coefficient d.

We utilize an open-source, editable PSO algorithm implemented in MATLAB by Mostapha (2016), and then begin the process of tuning parameters and hyperparameters. Pace et al. (2021) recommended a swarm size of nine times the number of variables. Since there are 13 variables, an appropriate swarm size is 117. However, very large swarm sizes slow down the algorithm and sometimes lower performance. So, four different swarm sizes were selected, varying from 60 to 140. For the number of iterations, a conservative number of 300 was chosen, with an additional stopping criterion of no change in the solution with a tolerance of 10^{-4} for 50 iterations. A hyperparameter selection strategy developed by Zhang et al. (2014) allows for the selection of one value μ that calculates corresponding values of ω, c_p, c_g, and d. So, instead of selecting various combinations of the three hyperparameters, μ varies from 0.6 to 0.8, and the hyperparameters are calculated from μ. In this strategy, c_p and c_g are equal. The strategy was tested alongside three previous hyperparameter optimization strategies on six benchmark functions.

All combinations of μ and n_s were compared totaling 20 options, with the number of iterations being monitored. The comparison was performed for magnitudes M_w = 4, 6, and 8. None of the combinations of hyperparameters resulted in an inversion taking more than 150

iterations, so the stopping criterion was unchanged. Table 5 summarizes the results from the first round of comparisons.

Table 5. Best Combinations of Hyperparameters from First Comparison

Magnitude, **M**	μ and n_s corresponding to minimum objective function value	
4	$\mu = 0.7$	$n_s = 140$
6	$\mu = 0.65$	$n_s = 120$
8	$\mu = 0.65$	$n_s = 140$

From Table 5, all the problems yielded best results for $\mu = 0.65$ or 0.7, and $n_s = 120$ or 140, a similar test was conducted with four options for μ equally spaced between 100 and 160 and three options for n_s equally spaced between 0.65 and 0.7. Table 6 summarizes the final hyper parameters used to complete the inversions.

Table 6. Hyperparameters used in the Final Inversions

Hyperparameter	**Value**
μ	0.675
ω	0.690
d	0.124
c_p	1.542
c_g	1.542
n_s	120

Results

Resulting Model Parameters

This section summarizes the resulting model parameters. Here, the mean of each model parameter is plotted with the standard deviation of the model parameter from the 50 iterations of each inversion, and the upper and lower constraints of each parameter are reflected in the figures.

Figure 2 shows the estimates of the stress parameter versus magnitude. The stress parameter was constrained between 10 bars and 600 bars and rounded to the nearest 5 bars to reduce the search space. As can be observed from Figure 2, the stress parameter increases

from $4 \leq M_w \leq 6.5$, and then decreases; the standard deviation of the stress parameter generally increases with magnitude. The greatest standard deviation of the stress parameter is approximately 25 bars.

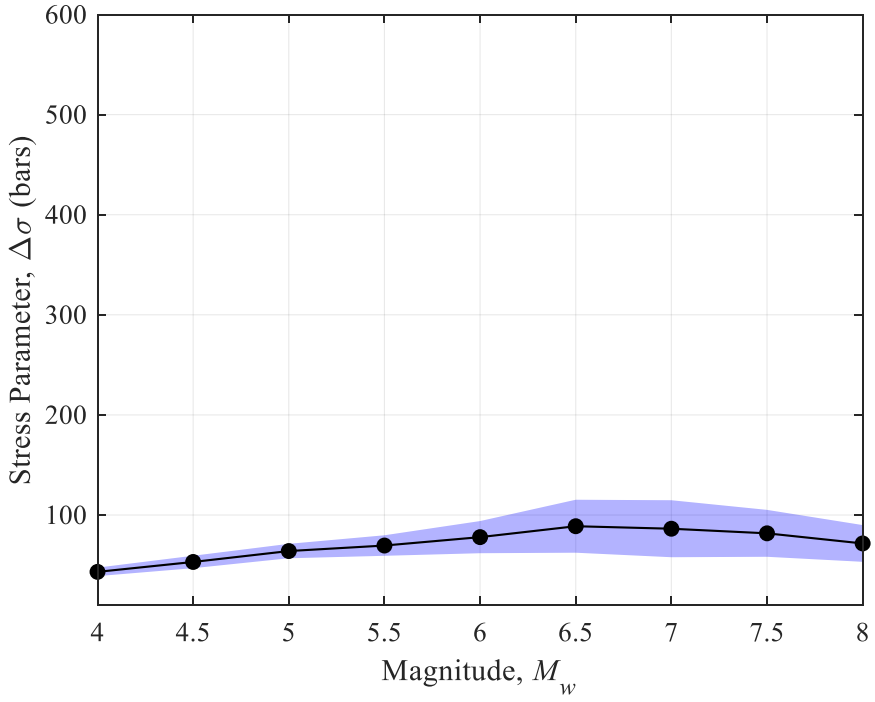

Figure 2. Stress Parameter Estimations from Magnitude-Specific Inversions

Figure 3 shows estimates of b_1 at the eight log-spaced frequencies varying from 0.1 Hz to 100 Hz for each magnitude-specific inversion. As mentioned before, in the evaluation of the model, a modified version of Akima's spline was used to evaluate b_1 in between the eight log-spaced frequencies; the interpolation method is accurately reflected in Figure 3. For all inversions, b_1 was constrained between -1.3 and -0.6. As can be observed from Figure 3, b_1 changes the most between 0.1 and 0.25 Hz, and has a higher standard deviation for the larger magnitudes.

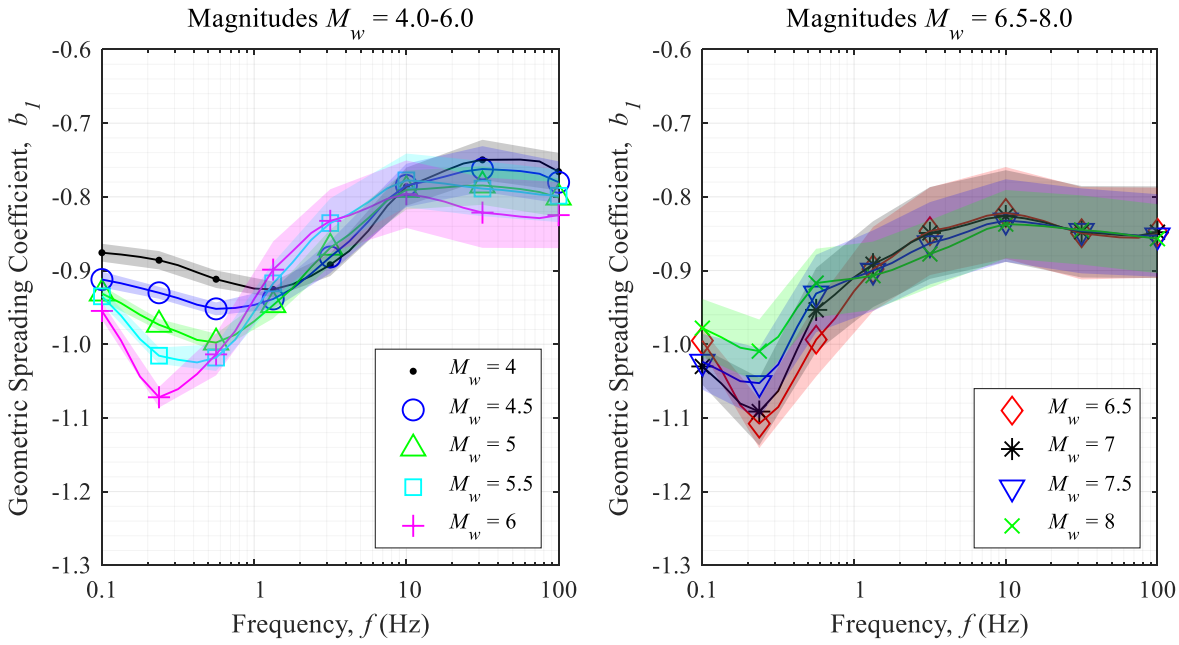

Figure 3. b_1 Estimations versus Frequency from Magnitude-Specific Inversions

Figure 4 shows estimates of b_2 for each magnitude-specific inversion. For all inversions, b_2 was constrained between -1 and 0.5. As can be observed from Figure 4, b_2 has a linear increase with magnitude from -0.75 up to -0.25, and roughly the same standard deviation across all magnitudes.

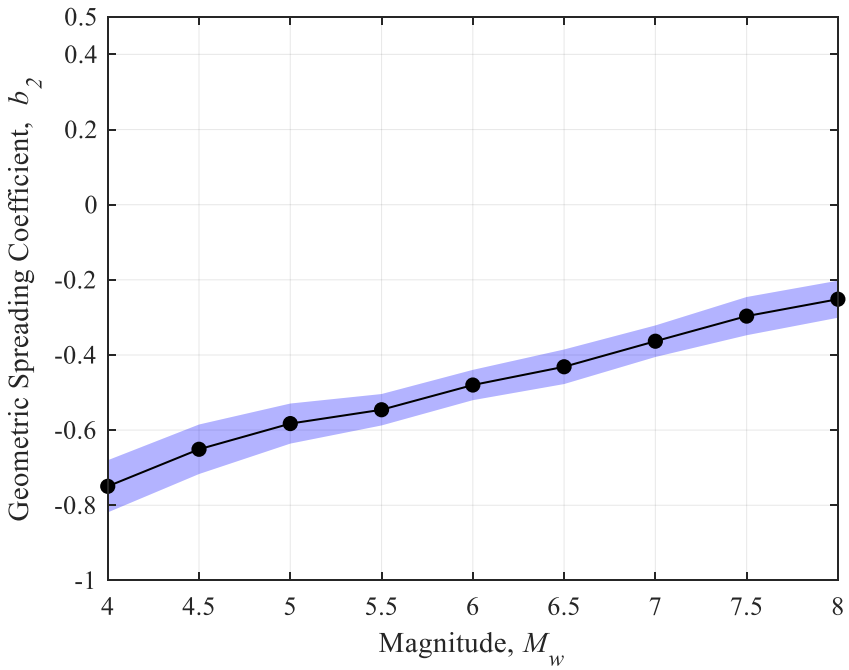

Figure 4. b_2 Estimations versus Magnitude from Magnitude-Specific Inversions

Figure 5 shows estimations of h for each magnitude-specific inversion. h was constrained between 0 and 30 km. As can be observed from Figure 5, h increases with magnitude, and has a slowly increasing standard deviation with magnitude.

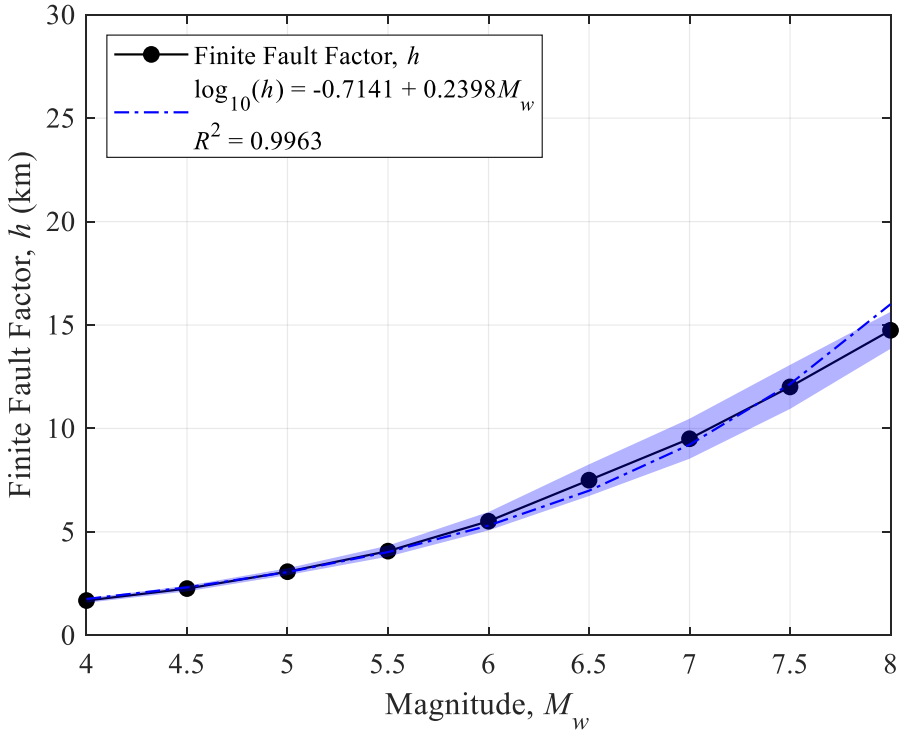

Figure 5. h Estimations from Magnitude-Specific Inversions

Figure 6 shows estimations of Q_0 and η for each magnitude-specific inversion. Since Q_0 and η together form the quality function, the parameters are highly correlated with each other. For all inversions, Q_0 was constrained between 250 and 800, and η was constrained between 0.35 and 0.75. As can be observed from Figure 6, Q_0 slowly increases with magnitude from 450 to 575, whereas η remains nearly constant at 0.555 for all magnitudes.

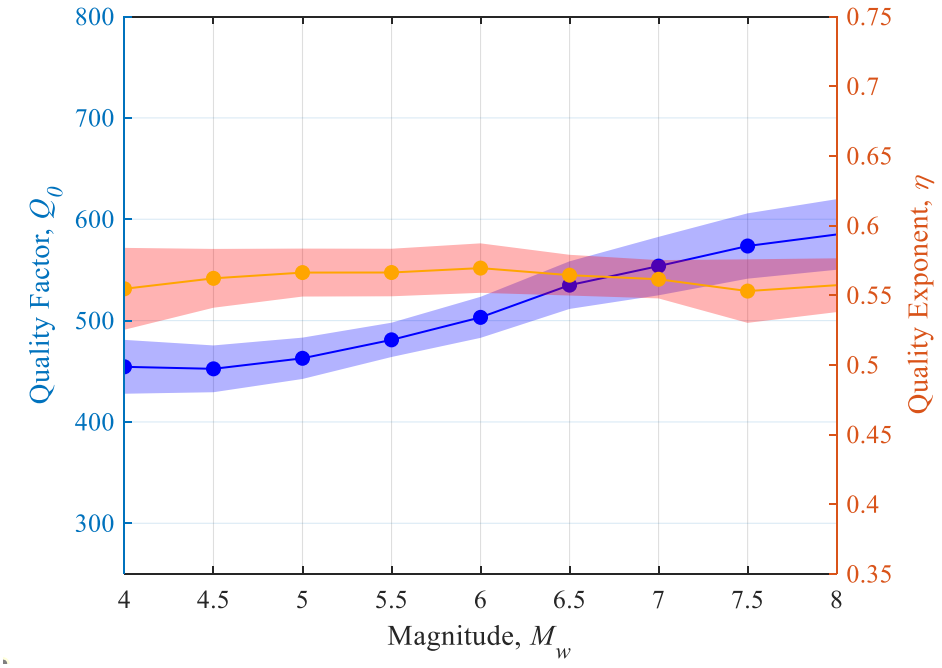

Figure 6. Q_0 and η Estimations from Magnitude-Specific Inversions

Figure 7 shows the quality function for each magnitude-specific inversion resulting from the estimates of Q_0 and η in Figure 6. As can be observed from Figure 7, the quality function slightly increases with magnitude.

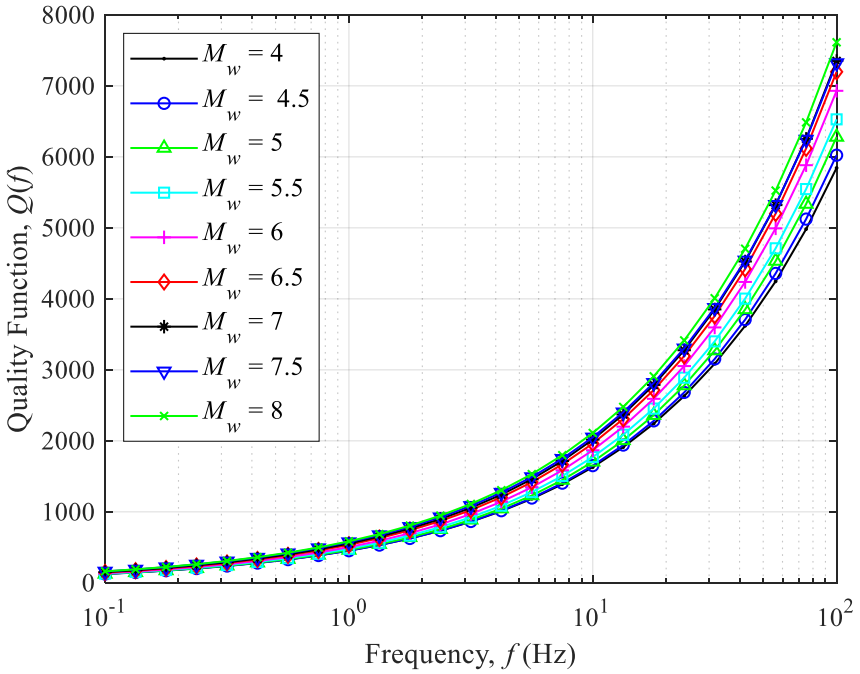

Figure 7. $Q(f)$ Estimations from Magnitude-Specific Inversions

Table 7 summarizes the resulting model parameters from the magnitude-specific inversions, except for b_1, which is shown in Table 8.

Table 7. Resultant Model Parameters from Inversion (Except b_1)

Magnitude, M	$\Delta\sigma$	b_2	h	Q_0	η
4.0	43.2	-0.75	1.68	454	0.55
4.5	53.1	-0.65	2.26	452	0.56
5.0	64	-0.58	3.08	463	0.57
5.5	69.5	-0.55	4.07	481	0.57
6.0	77.9	-0.48	5.52	503	0.57
6.5	88.8	-0.43	7.50	535	0.56
7.0	86.3	-0.36	9.50	554	0.56
7.5	81.7	-0.30	12.01	574	0.55
8.0	71.6	-0.25	14.75	585	0.56

Table 8. Resultant b_1 (frequency-dependent)

Magnitude, M	$b_1(f)$							
	Frequency, *f* (Hz)							
	0.1	**0.2371**	**0.5623**	**1.3335**	**3.1623**	**10**	**31.6228**	**100**
4.0	-0.88	-0.89	-0.91	-0.93	-0.89	-0.79	-0.75	-0.77
4.5	-0.91	-0.93	-0.95	-0.94	-0.88	-0.78	-0.76	-0.78
5.0	-0.93	-0.97	-1.00	-0.95	-0.87	-0.79	-0.78	-0.80
5.5	-0.94	-1.02	-1.02	-0.92	-0.84	-0.78	-0.79	-0.80
6.0	-0.95	-1.07	-1.01	-0.90	-0.83	-0.80	-0.82	-0.82
6.5	-1.00	-1.11	-0.99	-0.90	-0.85	-0.82	-0.85	-0.85
7.0	-1.03	-1.09	-0.95	-0.89	-0.85	-0.83	-0.85	-0.85
7.5	-1.02	-1.05	-0.93	-0.90	-0.86	-0.83	-0.85	-0.85
8.0	-0.98	-1.01	-0.92	-0.91	-0.88	-0.84	-0.85	-0.86

Resulting Model Compared to The Median of NGA-East GMMs

This section compares the results of this study to the median NGA-East GMMs in multiple ways. Figure 8 shows the PSA predicted from the stochastic model compared to the PSA predicted from the median NGA-East GMMs versus structural frequency f at ruptures distances R_{rup} = 1, 4, 17, 72, 304, and 788 km for magnitudes M_w = 4, 6, and 8. Figure 8 also

includes σ, which is the total or ergodic standard deviation of the median PSA predicted by the NGA-East GMMs in log units:

$$\sigma = \sqrt{{\sigma_{within-GMMs}}^2 + {\sigma_{between-GMMs}}^2} \quad (12)$$

where $\sigma_{within\text{-}GMMs}$ is the average within-model uncertainty in median predictions of the NGA-East models and $\sigma_{between\text{-}GMMs}$ is the uncertainty between the NGA-East GMMs (Al Atik, 2015). Figure 8a, 8b, and 8c show the PSA versus frequency at six different distances for magnitude M_w = 4, M_w = 6, and M_w = 8, respectively.

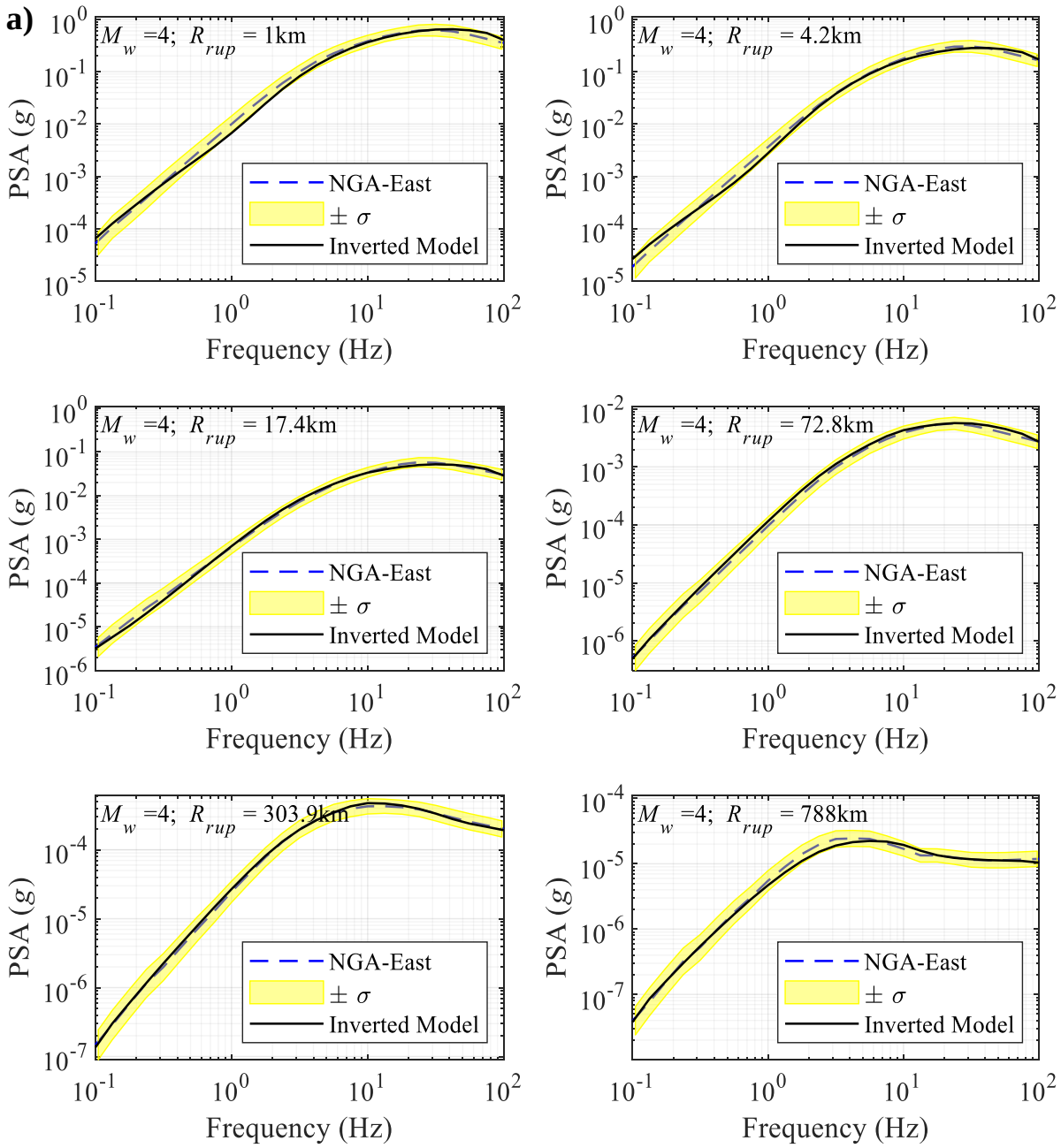

Figure 8. Comparison of the PSA versus structural frequency from the median NGA-East GMMs and this study. a) M_w = 4, b) M_w = 6, c) M_w = 8. The highlighted area is the total or ergodic standard deviation of the median NGA-East GMMs.

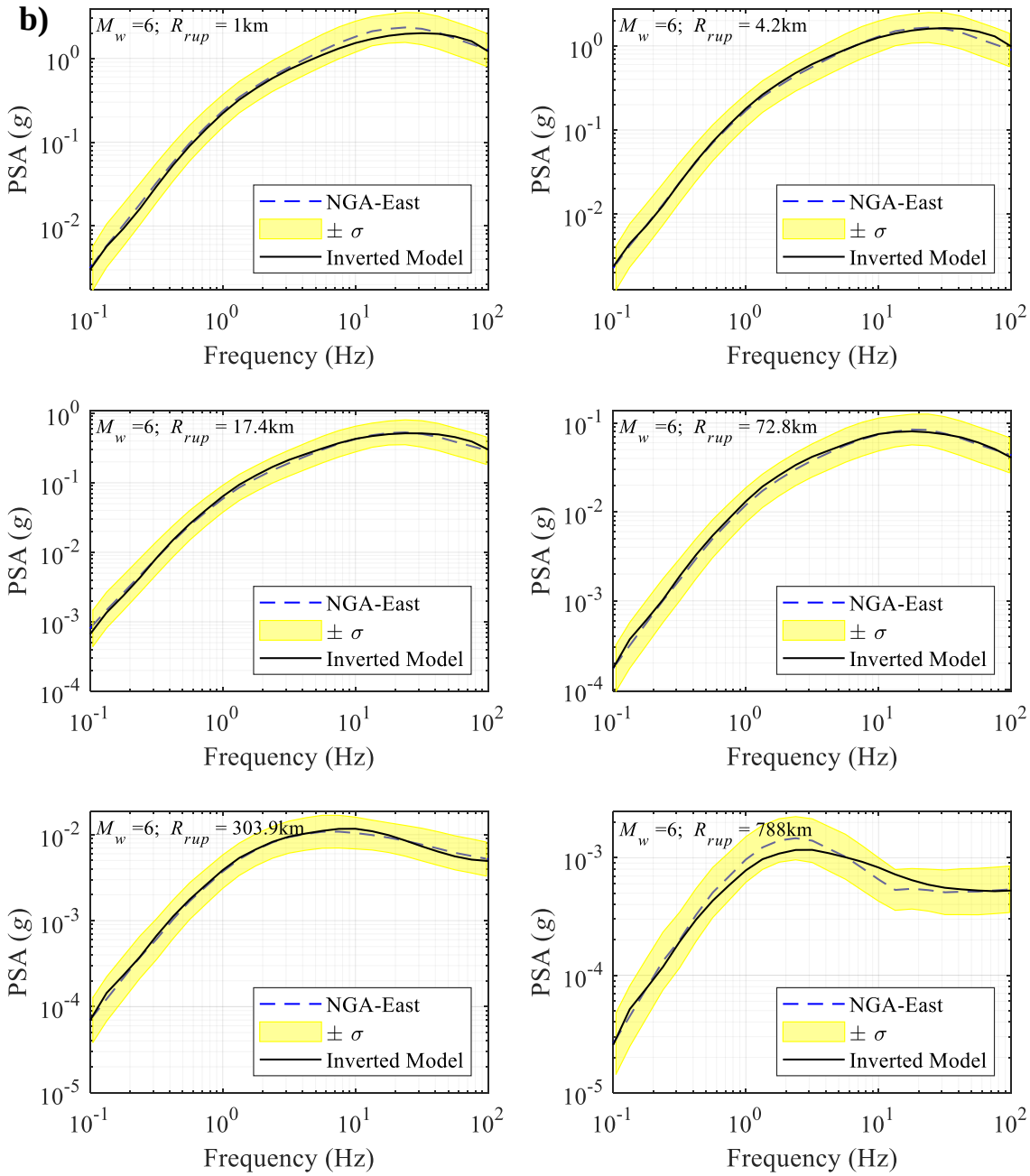

Figure 8. (continued) Comparison of the PSA from the median NGA-East GMMs and this study. a) M_w = 4, b) M_w = 6, c) M_w = 8. The highlighted area is the total or ergodic standard deviation of the median NGA-East GMMs.

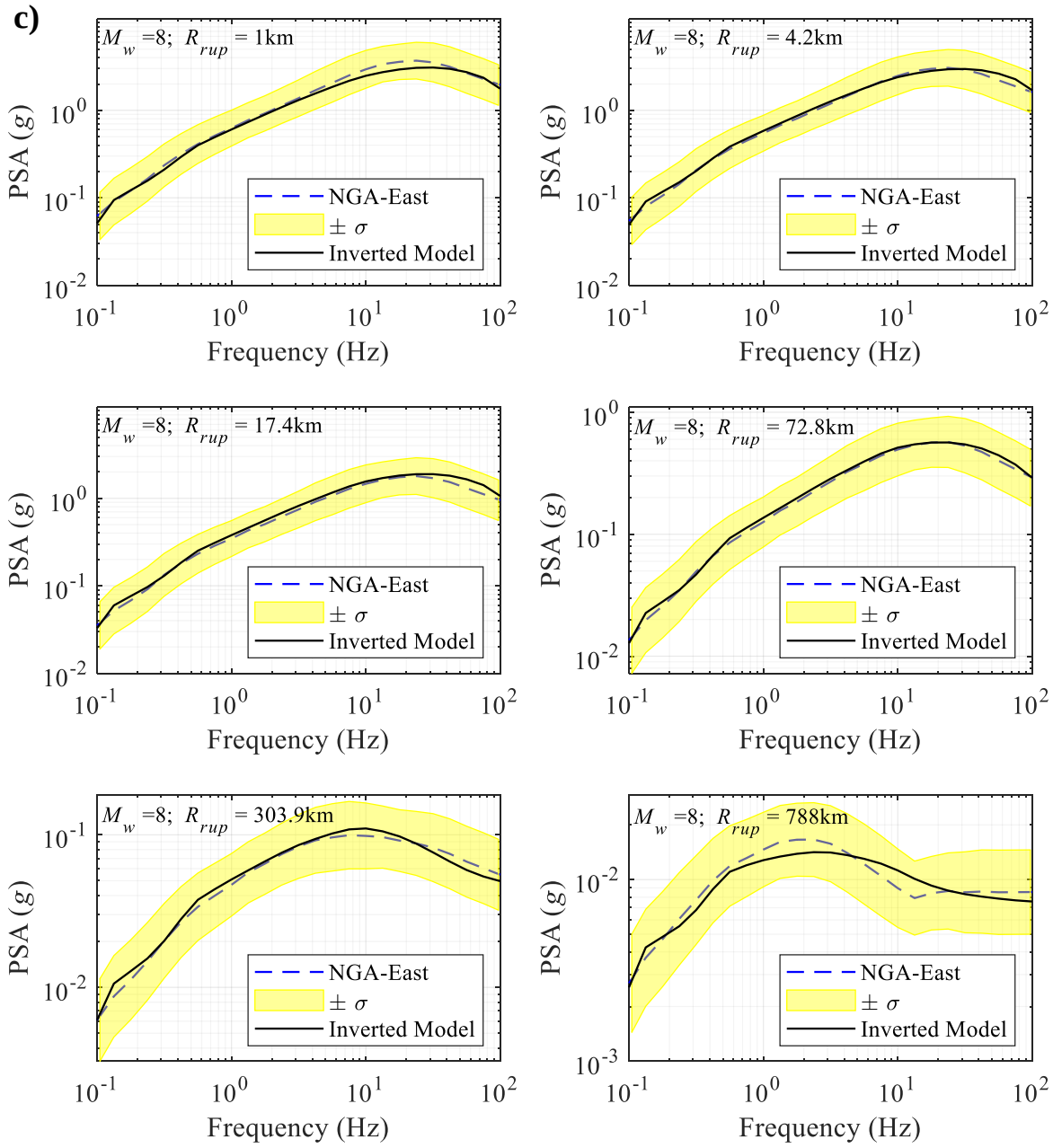

Figure 8. (continued) Comparison of the PSA from the median NGA-East GMMs and this study versus structural frequency. a) M_w = 4, b) M_w = 6, c) M_w = 8. The highlighted area is the total or ergodic standard deviation of the median NGA-East GMMs.

From Figure 8, the stochastic model from this study agrees best with the median NGA-East GMMs for the mid-range distances (approximately 17 km ≤ R_{rup} ≤304 km). From Figure 8c, the stochastic model has an odd shape compared to the model for the lower

magnitudes shown in Figure 8a and 8b. However, the stochastic model still agrees well with the median NGA-East GMMs for magnitude M_w = 8, well below the standard deviation.

When developing the stochastic model, it was speculated that the sharp increases and decreases shown in Figure 8c for 0.1 Hz $\leq f \leq$ 0.5 Hz was from the discretization of b_1; however, this shape persisted with several different b_1 models, including a single value for b_1 for all frequencies. Figure 9 compares the PSA from the median NGA-East GMMs and this study versus magnitude for rupture distances R_{rup} = 1, 4, 17, 73, 304, and 788 km, and structural frequencies f = 0.1, 1, 10 and 100 Hz.

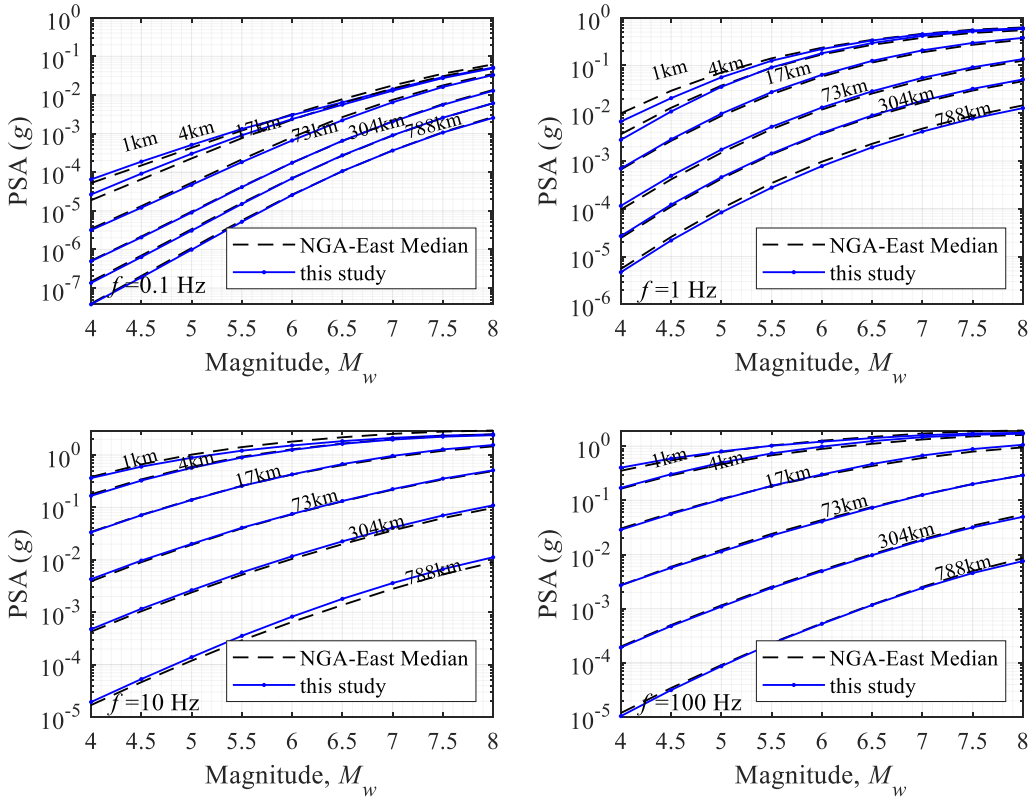

Figure 9. Comparison of the PSA from the median NGA-East GMMs and this study versus magnitude at rupture distances R_{rup} = 1, 4, 17, 73, 304, and 788 km, and structural frequencies f = 0.1, 1, 10 and 100 Hz.

From Figure 9, at a structural frequency of f = 0.1 Hz (top left of Figure 9), the best agreement for all magnitudes occurs for $R_{rup} \geq$ 73 km. At a structural frequency of f = 1 Hz

(top right of Figure 9), the best agreement for all distances occurs for $M_w \geq 6$. At a structural frequency of f = 10 Hz (bottom left of Figure 9), the best agreement for all magnitudes occurs for 73 km $\leq R_{rup} \leq$ 304 km. At a structural frequency of f = 100 Hz (bottom right of Figure 9), the model agrees very well at all magnitudes and distances.

Figure 10 compares the PSA from the median NGA-East GMMs and this study versus distance at magnitudes M_w = 4, 5, 6, 7, and 8 and structural frequencies f = 0.1, 1, 10, and 100 Hz. As can be observed from Figure 10, the agreement between the median NGA-East GMMs and the stochastic model increases with frequency for all magnitudes.

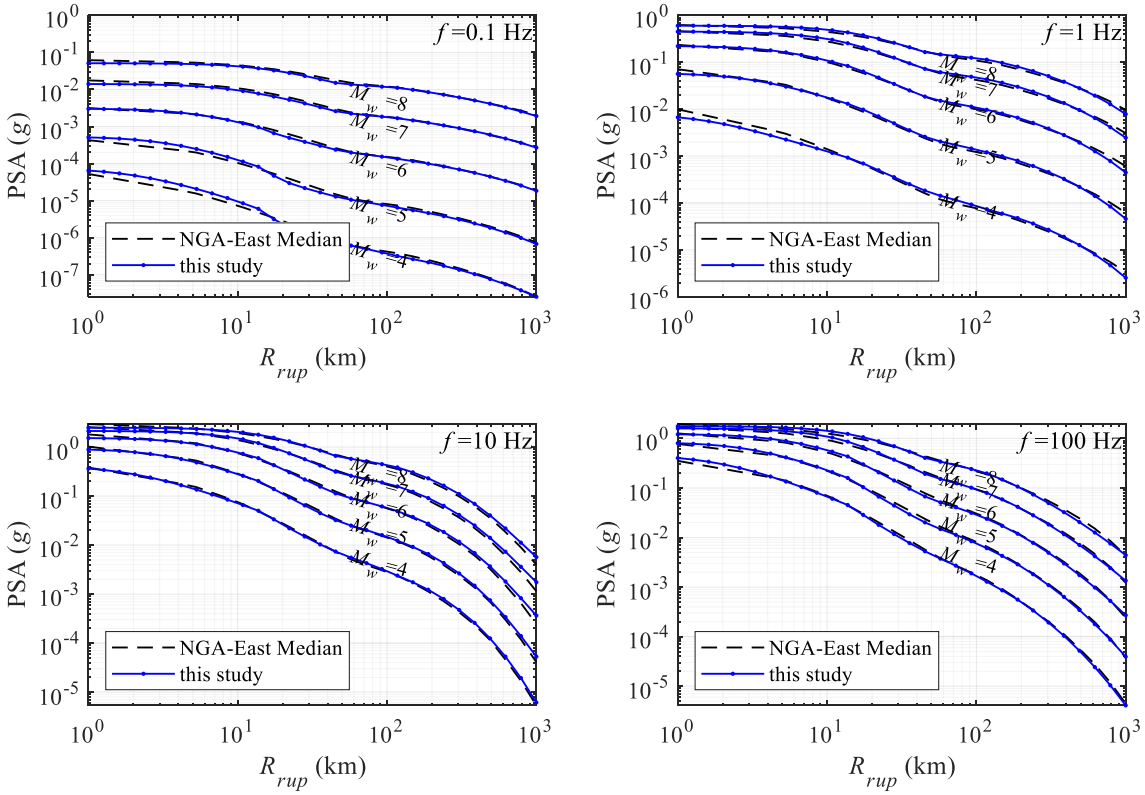

Figure 10. comparison of the PSA from the median NGA-East GMMs and this study versus distance at magnitudes M_w = 4, 5, 6, 7, and 8 and structural frequencies f = 0.1, 1, 10, and 100 Hz.

Residual Analyses

We perform residual analyses to investigate the proposed model's strengths and weaknesses. A natural log residual value is defined by:

$$r_{psa} = \ln(G) - \ln(S) \quad (13)$$

where G is the value of PSA observed from the median NGA-East GMMs, and S is the PSA predicted from the stochastic model using the resulting seismological parameters. When G and S are the same, $r_{psa} = 0$. Figure 11 shows the mean r_{psa} versus frequency for M_w = 4.0, 4.5, 5.5, 6.5, 7.5, and 8.0 across all 30 rupture distances included in the study.

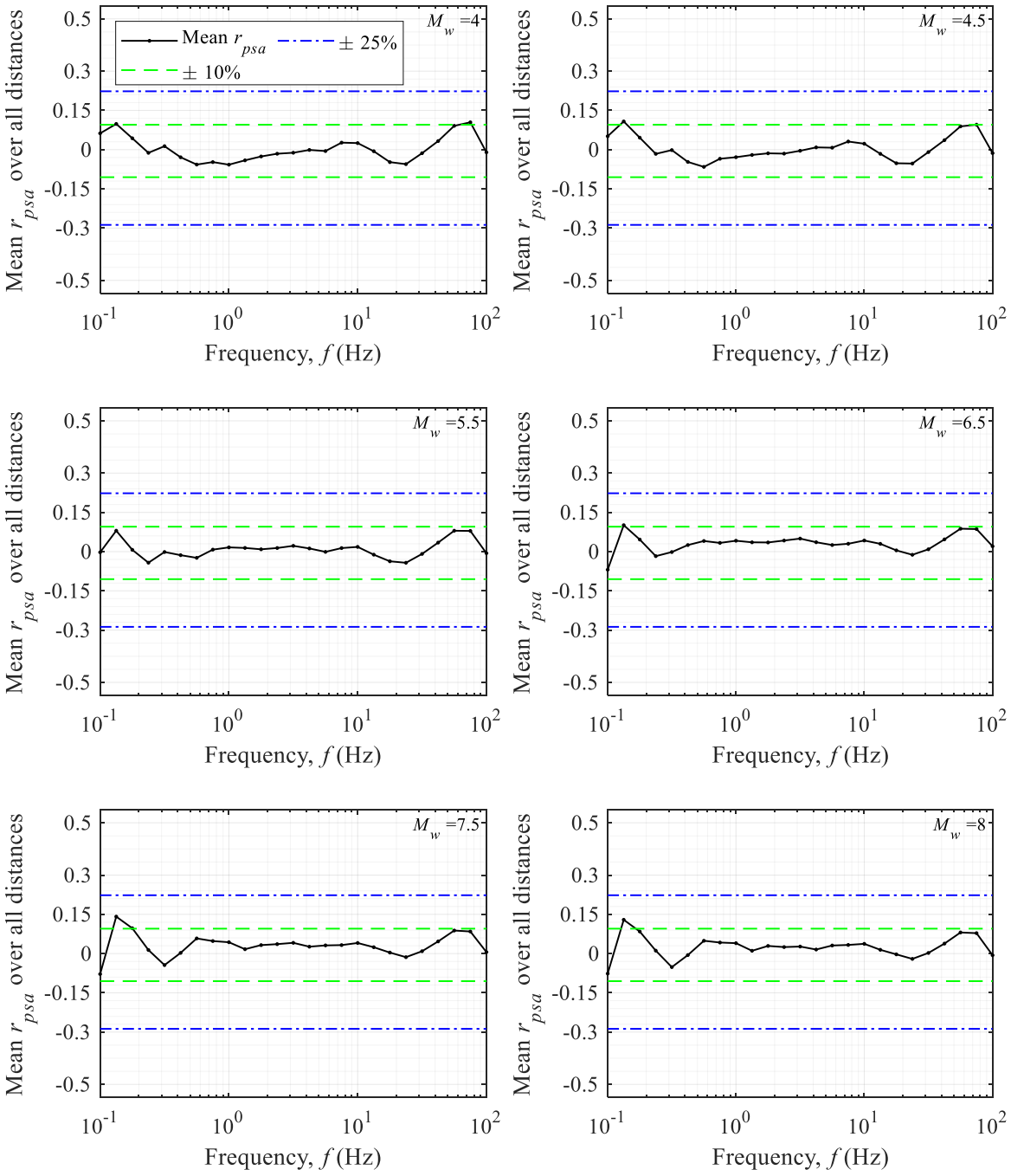

Figure 11. the mean r_{psa} versus structural frequency for M_w = 4, 4.5, 5.5, 6.5, 7.5, and 8 across all rupture distances.

Figure 12 shows the magnitude, frequency, and distance combinations for which the difference between PSA values predicted by the stochastic model and the median PSA of NGA-East GMMs is less than 10%. As can be observed from Figure 12, the larger the magnitude, the more predictions fall within the 10% difference.

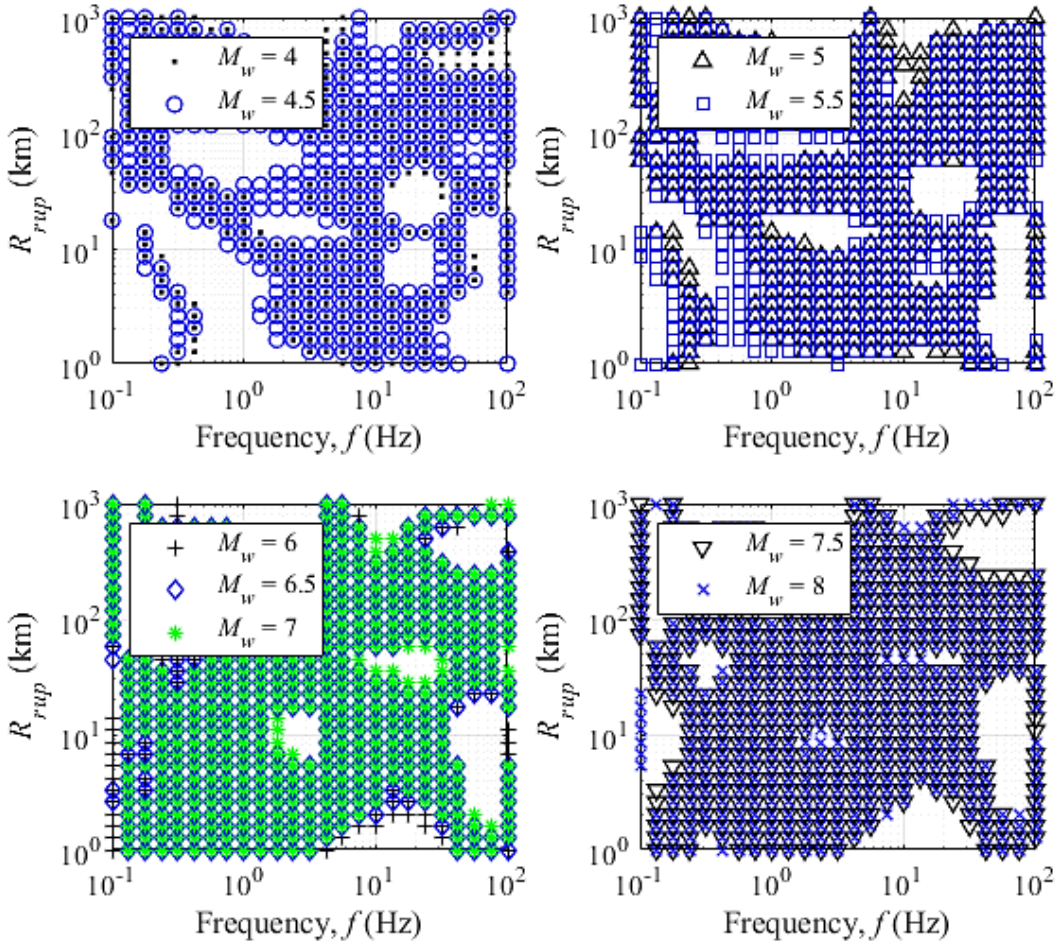

Figure 12. Magnitude, rupture distance, and structural frequency combinations for which the percent difference between the PSA stochastically predicted from the model in this study and the PSA from the median of the NGA-East GMMs are within 10%.

Figure 13 shows the magnitude, frequency, and distance combinations for which the difference between PSA values predicted by the stochastic model and the median PSA of NGA-East GMMs is more than 25%. As can be observed from Figure 13 shows a similar trend as Figure 12, with the most values greater than 25% difference shown with magnitudes

M_w = 4 and 4.5. The greatest misfit is present at the edges of the problem, with very low frequencies and very short distances or very high frequencies with very long distances.

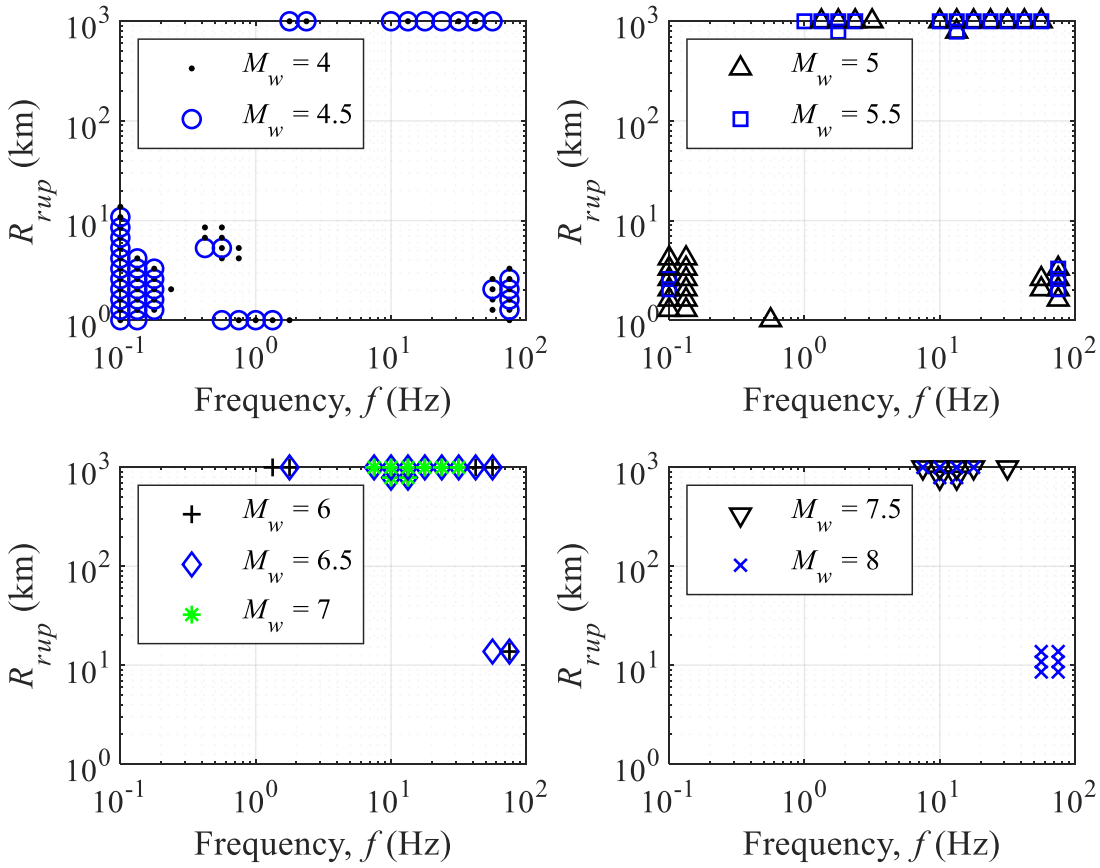

Figure 13. Magnitude, rupture distance, and structural frequency combinations for which the percent difference between the PSA stochastically predicted from the model in this study and the PSA from the median of the NGA-East GMMs is greater than 25%.

Conclusions

We used particle swarm optimization (PSO) to invert weighted geometric mean estimates of horizontal response-spectral acceleration from the empirical NGA-East GMMs to estimate a consistent set of seismological parameters that can be used along with an equivalent point-source stochastic model to mimic the general scaling characteristics of these GMMs. The inversion is performed for events of $\mathbf{M} = 4.0 - 8.0$, $R_{RUP} = 1 - 1000$ km, $T = 0.01 - 10$ sec ($f = 0.1 - 100$ Hz), NEHRP BA site conditions ($V_{S30} = 3000$ m/sec).

Several elements of the seismological model were fixed to values obtained in recent studies in the inversion (Table 3). These included the source-spectral shape (Brune 1971, 1972), the source velocity and source density (Atkinson and Boore, 2014), the geometric spreading transition distances for the geometrical spreading model (Boore and Thompson, 2015), the path duration (Boore and Thompson, 2015), and the site-amplification factors (Boore and Thompson, 2015). All other parameters in Table 3 were fit in the inversion. The results are summarized in Tables 7 and 8.

As part of the inversion, we obtained the geometric spreading for $R_{RUP} \leq 50$ km to be consistent with a distance decay of about $R^{-0.75}$ to $R^{-1.11}$ for M_w ranging from 4.0 to 8. The stress parameter is a function of magnitude which increases from 43.2 bars at M_w 4.0 to 88.8 bars at M_w 6.5 and then decreases with increasing magnitude to about 71 bars at M_w 8.0. The agreement over all magnitudes and distances evaluated in this study is generally within 10% for almost all magnitudes and frequencies.

Data and Resources

The ground motion characterization (GMC) tool for the CEUS GMMs is available at https://www.risksciences.ucla.edu/nhr3/ngaeast-gmtools from Goulet et al. (2018). The PSO algorithm used is available at https://yarpiz.com/440/ytea101-particle-swarm-optimization-pso-in-matlab-video-tutorial from Mostapha (2016). All codes used in performing the inversions, gathering inversion results, and developing figures in this study are available at https://github.com/cmmore11/Inversion_NGA_East/.

References

Akima, Hiroshi, 1970. A new method of interpolation and smooth curve fitting based on local procedures, *Journal of the ACM*, **17**, 589–602.

Al Atik, L., 2015. NGA-East: *Ground-Motion Standard Deviation Models for Central and Eastern North America, PEER Reports 2015/07*. Pacific Earthquake Engineering Research Center, University of California, Berkeley, CA.

Aleardi, M., 2018. Using orthogonal Legendre polynomials to parameterize global geophysical optimizations: Applications to seismic-petrophysical inversion and 1D elastic full-waveform inversion, *Geophysical Prospecting*, **67(2)**, 331-348.

Anderson J. G., 1986. Implication of attenuation for studies of the earthquake source, In: Earthquake Source Mechanics, Geophysics Monograph Series, Vol. 37, S. Das, J. Boatwright, and C.H. Scholz (Eds.), pp. 311−318, American Geophysical Union. Washington, D.C.

Anderson J. G., 1991. A preliminary descriptive model for the distance dependence of the spectral decay parameter in southern California, *Bulletin of the Seismological Society of America*, **81(6)**, 2186–2193.

Anderson, J. G., and S. E. Hough, 1984. A model for the shape of the Fourier amplitude spectrum of acceleration at high frequencies, *Bulletin of the Seismological Society of America*, **74(5)**, 1969–1993.

Anderson J.G., Lee, Y., Zeng, Y., and Day, S., 1996. Control of strong motion by the upper 30 meters, *Bulletin of the Seismological Society of America*, **86(6)**, 1749–1759.

Atkinson, G. M., 1993. Earthquake Source Spectra in Eastern North America, *Bulletin of the Seismological Society of America* **83(6)**, 1778–1798.

Atkinson G.M., 2004. Empirical attenuation of ground-motion spectral amplitudes in southeastern Canada and the northeastern United States, *Bulletin of the Seismological Society of America*, **94**, 1079–1095.

Atkinson G.M., Boore, D.M., 2014. The attenuation of Fourier amplitudes for rock sites in eastern North America, *Bulletin of the Seismological Society of America*, **104**, 513–528.

Atkinson, G. M., and Silva, W. J., 2000. Stochastic modeling of California ground motions, *Bulletin of the Seismological Society of America*, **90(2)**, 255–274.

Boatwright J., Seekins, L., 2011. Regional spectral analysis of three moderate earthquakes in northeastern North America, *Bulletin of the Seismological Society of America*, **101(4)**, 1769–1782.

Boore, D. M., 2003. Prediction of ground motion using the stochastic method, *Pure Applied Geophysics*, **160**, 635–676.

Boore, D. M., 2012. Updated Determination of Stress Parameters for Nine Well-Recorded Earthquakes in Eastern North America, *Seismological Research Letters* **83(1)**, 190–199.

Boore, D. M., and Thompson, E. M., 2014. Path duration for use in the stochastic-method simulation of ground motions, *Bulletin of the Seismological Society of America*, **104**, 2541–2552.

Boore, D. M., and Thompson, E. M., 2015. Revisions to some parameters used in stochastic method simulations of ground motion, *Bulletin of the Seismological Society of America*, **105**, 1029–1041.

Boore, D. M., Joyner, W. B., and T.E. Fumal, 1997. Equations for estimating horizontal response spectra and peak acceleration from Western North American earthquakes: A summary of recent work, *Seismological Research Letters*. **68**, 128–153.

Campbell, K. W., 2003. Prediction of strong ground motion using the hybrid empirical method and its use in the development of ground-motion (attenuation) relations in eastern North America, *Bulletin of the Seismological Society of America*. **93**, 1012–1033.

Campbell, K. W., Hashash, Y. M. A., Kim, B., Kottke, A. R., Rathje, E. M., Silva, W. J., and J. P. Stewart, 2014. *Reference- rock site conditions for Central and Eastern North America: Part II – Attenuation definition, PEER Report 2014/12*, Pacific Earthquake Engineering Research Center, University of California, Berkeley, CA.

Dabaghi, M., and Der Kiureghian, A., 2014. *Stochastic Modeling and Simulation of Near-Fault Ground Motions for Performance-Based Earthquake Engineering, PEER Report 2014/20*. Pacific Earthquake Engineering Research Center, University of California, Berkeley, CA.

Engelbrecht, A. P., 2007. *Computational Intelligence: An Introduction*, 2nd Ed., Wiley, Hoboken, NJ.

Goulet, C. A., Bozorgnia, Y., and Abrahamson, N. A., 2015. *PEER NGA-East: Median Ground Motion Models for the Central and Eastern North America Region, Tech. Rep. Pacific Earthquake Engineering Research Center (PEER) 2015/04*. Berkeley, California.

Goulet, C. A., Bozorgnia, Y., Abrahamson, N. A., Kuehn, N., Atik, L. A., Youngs, R., and Graves, R., 2018. *Central and Eastern North America Ground-Motion Characterization - NGA-East Final Report, Tech. Rep. Pacific Earthquake Engineering Research Center (PEER) 2018/08*. Berkeley, California.

Goulet, C. A., Bozorgnia, Y., Abrahamson, N. A., Kuehn, N., Atik, L. A., Youngs, R., and Graves, R., 2018. *NGA-East Ground Motion Characterization Tool (GMC)*, software, https://www.risksciences.ucla.edu/nhr3/ngaeast-gmtools.

Gregor, N. J., Silva, W. J., Wong, I. G., and Youngs, R., 2002. Ground Motion Attenuation Relationship for Cascadia Subduction Zone Megathrust Earthquakes Based on a Stochastic Finite Fault Model, *Bulletin of the Seismological Society of America* **92(5)**, 1923–1932.

Hanks, T. C., and Kanamori, H., 1979. A Moment Magnitude Scale, *Journal of Geophysical Research* **84(5)**, 2348–2350.

Ionita, C., 2019. Makima Piecewise Cubic Interpolation, blog post, 29 April 2019, https://blogs.mathworks.com/cleve/2019/04/29/makima-piecewise-cubic-interpolation/ (last accessed 18 January 2023).

Kottke, A. R., and Rathje, E. M., 2008. *Technical Manual for Strata, PEER Rept. No. 2008/10*, Pacific Earthquake Engineering Research Center, University of California, Berkeley, California

Koza, J. R., 1992. *Genetic programming: on the programming of computers by means of natural selection*, Massachusetts Institute of Technology Press, Cambridge, MA.

Kramer, S. L., 1996. *Geotechnical Earthquake Engineering*, Prentice Hall, Upper Saddle River, 86-93.

Menke, W., 2018. *Geophysical Data Analysis: Discrete Inverse Theory*, 4th Ed., Academic Press, London.

Lagos, S.R., and Velis, D. R., 2018. Microseismic event location using global optimization algorithms: An integrated and automated workflow. *Journal of Applied Geophysics*. **149**, 18-24.

Mostapha, K. H., 2016. Particle Swarm Optimization (PSO) in Matlab – Video Tutorial (URL: https://yarpiz.com/440/ytea101-particle-swarm-optimization-pso-in-matlab-video-tutorial), Yarpiz.

Pace, F., Santilano, A., and Godio, A, 2021. A Review of Geophysical Modeling Based on Particle Swarm Optimization. *Surveys in Geophysics*. **42**, 505–549.

Pezeshk, S., A. Zandieh, and B. Tavakoli, 2011. Hybrid empirical ground-motion prediction equations for Eastern North America using NGA models and updated seismological parameters, *Bulletin of the Seismological Society of America.* **101(4)**, 1859-1870.

Pezeshk, S., A. Zandieh, K. W. Campbell, and B. Tavakoli, 2015. Ground-motion prediction equations for CENA using the hybrid empirical method in conjunction with NGA-West2 empirical ground-motion models, in *NGA-East: Median Ground-Motion Models for the Central and Eastern North America Region*, *PEER Rept. No. 2015/04*, Chapter 5, Pacific Earthquake Engineering Research Center, University of California, Berkeley, California, 119–147.

Rader, D. J., 2010. Deterministic Operations Research: Models and Methods in Linear Optimization. John Wiley and Sons, Inc, Hoboken.

Rathje, E. M., and Ozbey, M. C., 2006. Site-Specific Validation of Random Vibration Theory-Based Seismic Site Response Analysis, *Journal of Geotechnical and Geoenvironmental Engineering*, **132(7)**, 911-922.

Rathje, E. M., and Kottke, A. R., 2008. Procedures for Random Vibration Theory Based Seismic Site Response Analyses. Rockville, MD: Nuclear Regulatory Commission.

Silva, W. J., Abrahamson, N. A., Toro, G., and Constantino, C., 1997. Description and validation of the stochastic ground motion model. Unpublished report prepared for the Brookhaven National Laboratory. Brookhaven National Laboratory, Upton, NY.

Yenier, E., and G. M. Atkinson (2015a). Regionally adjustable generic ground-motion prediction equation based on equivalent point-source simulations: Application to central and eastern North America, *Bull. Seismol. Soc. Am.* **105**, 1989–2009.

Zandieh, A., Pezeshk, S., and Campbell, K. W., 2018. An equivalent point-source stochastic simulation of the NGA-West2 ground-motion prediction equations, *Bulletin of the Seismological Society of America* **108(2)**, 815–835.

Zhang, W., Ma, D., Wei, J., and Liang, H., 2014. A parameter selection strategy for particle swarm optimization based on particle positions, *Expert Systems with Applications*, **41(7)**, 3576-4174.

Chapter 3: A Seismological Method for Estimating the Long-Period Transition Period TL in the Seismic Building Code

Abstract

Many changes have been made to the design response spectrum used in the ASCE 7 Standard in recent years. One parameter that has not been investigated or re-visited since its first appearance in FEMA 450-1/2003 is the long-period transition period parameter, T_L. The long-period transition period parameter was introduced and defined as the corner period that marks the transition from the constant velocity to the constant displacement segments of the design response spectrum. The long-period transition period parameter is primarily important for long-period structures such as high-rise buildings and bridges. The most current estimation of T_L used in engineering design standards is loosely based on a correlation between modal magnitude M_w and T_L that does not account for stress drop $\Delta\sigma$ or the crustal velocity in the source region β. This study aims to include both $\Delta\sigma$ and β in its estimation of T_L. Modal magnitude is obtained from disaggregation data from the 2018 National Seismic Hazard Model (NSHM) for the conterminous United States (CONUS) and from the 2021 NSHM for Hawaii (HI). The parameter β is determined from previous literature. Then, inversion of ground motion models for Central and Eastern United States (CEUS) is used to determine $\Delta\sigma$ for CEUS events, and published information is used to determine $\Delta\sigma$ for Western United States (WUS) events and HI events. Then, the definition of the corner period is used to determine T_L. The results yield a generally more conservative (or longer) estimation of T_L than the estimation that is currently used in engineering design standards.

Introduction

A design response spectrum is used to determine the expected spectral acceleration of structures with different structural periods. For any earthquake, the response spectrum can be highly irregular. However, the idealized Newmark and Hall (1973) design response spectrum has three constant segments: spectral acceleration, spectral velocity, and spectral displacement. The T_L parameter marks the transition between the constant spectral velocity and the constant spectral displacement segments of the response spectrum. The results of this study estimate the long-period transition period parameter T_L. The T_L parameter is the natural period (in seconds) where the spectral acceleration S_a (g) decreases at a faster rate for $T > T_L$.

According to Bommer et al. (2000), the T_L parameter was sometimes considered and was sometimes ignored when constructing response spectra to be conservative. Before its inclusion in U.S. model building codes and design standards, T_L was estimated to be 4s (USNRC, 1973). However, Crouse et al. (2006) reported that a period of 4s was too low. T_L was first introduced to the U.S. model building code and design standards in FEMA 450-1: National Earthquake Hazard Reduction Program (NEHRP) Recommended Provisions for Seismic Regulations for New Buildings and Other Structures Provisions (hereafter called "FEMA 450-1") (BSSC, 2004a). According to Crouse et al. (2006) and FEMA 450-2, T_L can be approximated using the corner period on the Fourier spectrum T_c as:

$$T_L = T_{L(NEHRP)} \approx T_c \approx 10^{-1.25+0.3M_w} \quad (1)$$

$T_{L(NEHRP)}$ is the T_L parameter calculated from Equation 1 and used in FEMA 450-1, T_C is the corner frequency of the Fourier Amplitude spectrum, and M_w is the modal moment magnitude obtained from a probabilistic seismic hazard analysis (PSHA) disaggregation of 2% probability of exceedance in 50 years hazard (return period of 2,475 years) for spectral

acceleration at the spectral period of 2s for the conterminous United States (CONUS) and spectral period of 1s for Hawaii (HI) (BSSC, 2004b). Equation 1 was introduced in FEMA 450-1 and FEMA 450-2 and was used to develop the national map of the T_L parameter in the ASCE 7 Standard (BSSC, 2004a; BSSC, 2004b; ASCE, 2005). Crouse et al. (2006) state that Equation 1 is based on the seismic source model of Brune (1970); however, there is no calculable relationship between Brune's seismic source theory and Equation 1. Equation 1 does not account for the stress drop $\Delta\sigma$ or the crustal velocity of the source region β (hereafter called "source velocity"), whereas the Brune's seismic source model does. The determination of T_L has not been revisited or studied since its introduction. A formulation that includes regional seismological parameters would allow for a more customized estimation of T_L based on the geographic location. Further simplification was applied to Equation 1 to smooth T_L map boundaries by providing a single estimate for various magnitudes. Figure 1 compares Equation 1 $T_{L(NEHRP)}$ and the simplification used in the ASCE 7 Standard to develop $T_{L(NEHRP)sim}$ contour maps (BSSC, 2004b).

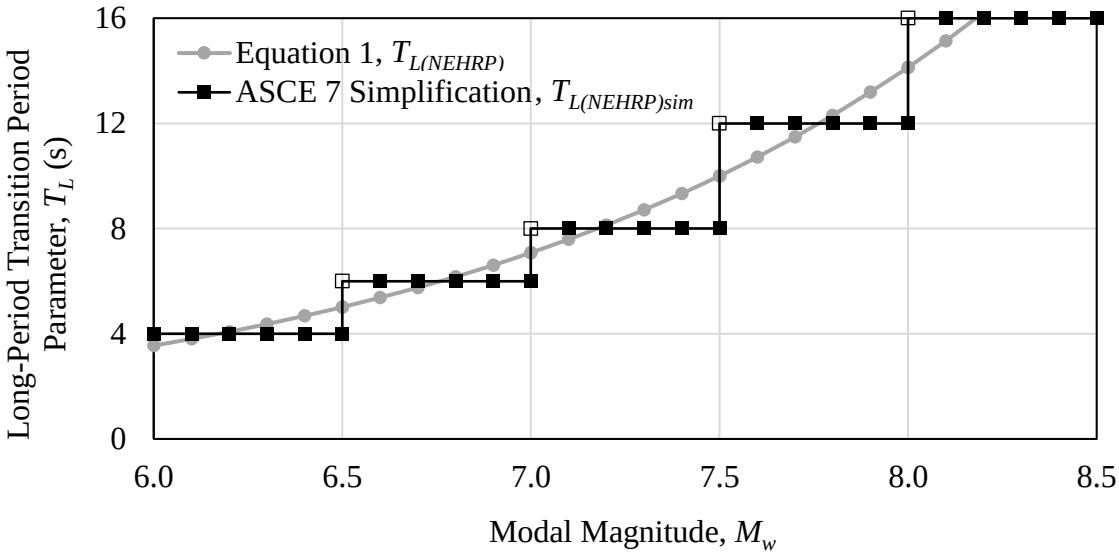

Figure 1.Comparison of Equation 1, $T_{L(NEHRP)}$ and Simplification Used in The ASCE 7 Standard, $T_{L(NEHRP)sim}$ (BSSC, 2004b; ASCE, 2005).

The simplification is meant to help smooth boundaries for the ASCE 7 Standard maps. However, the simplification is generally not conservative when compared to Equation 1. Underestimating T_L is not conservative because it causes the spectral acceleration to decrease prematurely with respect to the natural period of the structure. Figure 2 shows the ASCE 7 Standard existing maps for T_L for the CONUS and HI (ASCE, 2005; ASCE, 2016). The maps shown in Figure 2 were developed using the simplification shown in Figure 1.

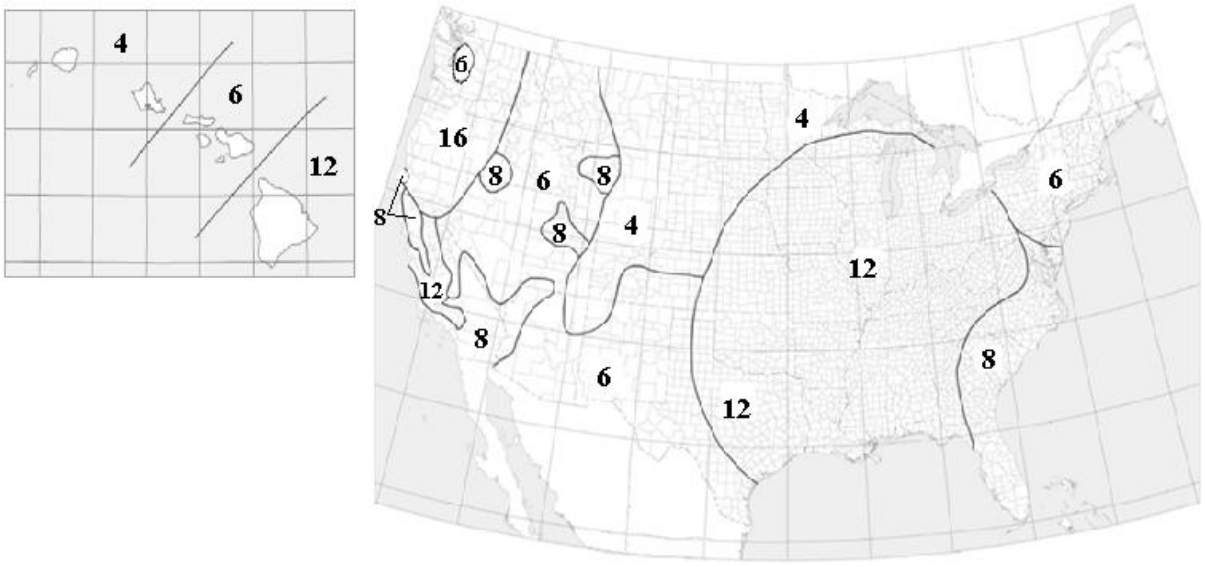

Figure 2. Mapped Long-Period Transition Period, T_L (seconds) for the CONUS (Figure 22-14 of BSSC, 2015) and Hawaii (Figure 22-16 of NEHRP, 2015). The Bold Numbers in Each Region Represent T_L for that Region.

Changes to the Design Response Spectrum in the U.S. Building Codes

Figure 3 shows the design response spectrum presented in FEMA 450-1 with T_L in bold; this is the first design response spectrum to include T_L in a U.S. model building code (BSSC, 2004a). The two-period design response spectrum shown in Figure 3 was the preferred design response spectrum used by the ASCE 7-05 Standard until the introduction of the multi-period response spectrum (MPRS) in the 2020 Edition of FEMA 450-1 and ASCE 7-22 (BSSC, 2020; ASCE, 2021). In MPRS, the shape of the response spectrum no longer adheres strictly to

constant acceleration, constant velocity, and constant displacement segments shown in Figure 3. The MPRS only approximately contains these three segments with smooth and continuous transitions in between.

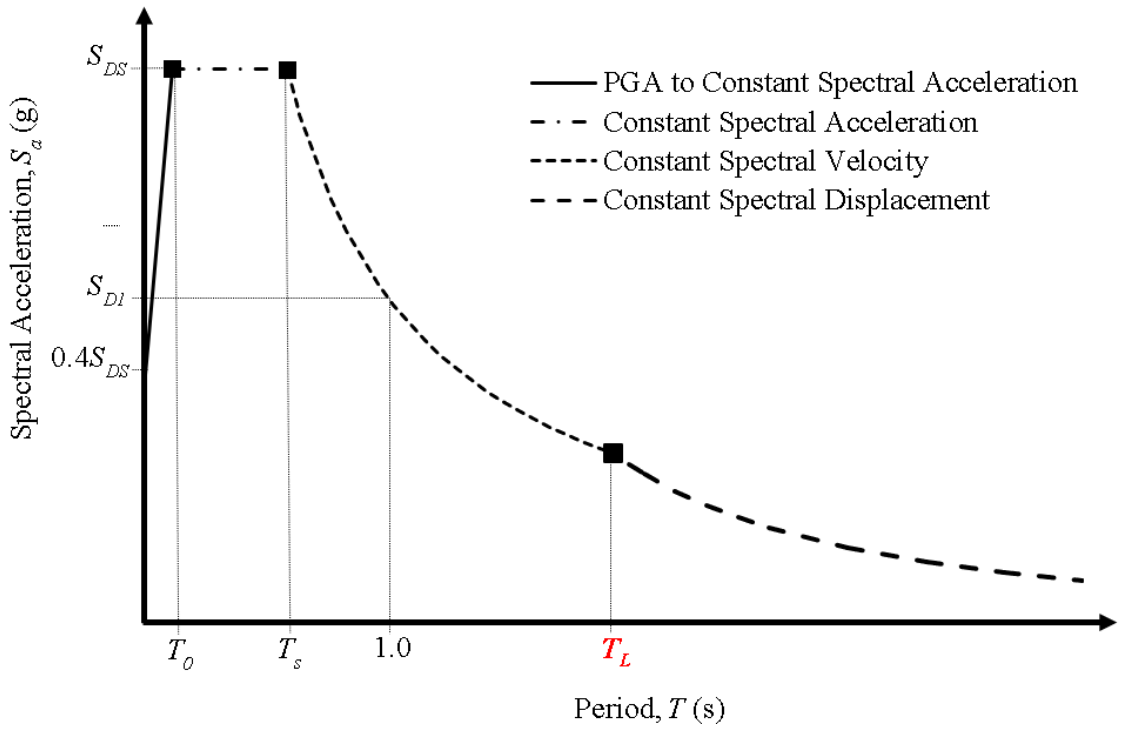

Figure 3. Generic Two-Period Response Spectrum, First Presented in FEMA 450-1 (BSSC, 2004a).

T_L is an important parameter in the two-period design response spectrum, because it affects both the constant spectral velocity and constant spectral displacement branches. While the two-period design response spectrum shown in Figure 3 is no longer the preferred criteria in the design requirements for FEMA 450-1, the parameter T_L is still a pertinent parameter, and is still calculated using the simplification of Equation 1 (BSSC, 2020).

Kircher & Associates (2015), in their critique of the ASCE 7-16 Standard, introduced the need for MPRS, particularly for the underestimation of ground motions at soft-soil sites (D and E). The short-term solution to address this issue was to require site-specific procedures for soft soil sites to determine S_1 (1s spectral acceleration at the NEHRP B/C site condition) or S_S (0.2s

spectral acceleration at the NEHRP B/C site condition) if they exceed certain levels. The USGS 2018 update of the U.S. National Seismic Hazard Model (NSHM) expanded the number of periods from just two to 22 to accommodate the development of an MPRS as well as the traditional two-period response spectrum (Petersen et al., 2019). There are eight soil site classes (the original NEHRP site classes and the boundary site classes B/C, C/D, and D/E). The introduction of the MPRS in FEMA 450-1 did not include changes to the determination of T_L; however, the use and the function of T_L in the construction of the response spectrum is different (BSSC, 2020; Kircher et al. 2019).

The MPRS is the preferred response spectrum with two exceptions: a site-specific ground motion analysis is performed, or the MPRS is not available for the site. If the MPRS is not available for the site, then the two-period design response spectrum shown in Figure 4 is used. The following block of text is a direct quote from Section 11.4.5.1 of ASCE 7-22 describing the development of the MPRS:

1. At discrete values of period, *T*, equal to 0.0s, 0.01s, 0.02s, 0.03s, 0.05s, 0.075s, 0.1s, 0.15s, 0.2s, 0.25s, 0.3s, 0.4s, 0.5s, 0.75s, 1.0s, 1.5s, 2.0s, 3.0s, 4.0s, 5.0s, 7.5s and 10s, the 5%-damped design spectral response acceleration parameter, S_a, shall be taken as 2/3 of the multi-period 5%-damped MCE_R response spectrum from the USGS Seismic Design Geodatabase for the applicable site class.
2. At each response period, *T*, less than 10s and not equal to one of the discrete values of period, *T*, listed in Item 1 above, S_a, shall be determined by linear interpolation between values of S_a, of Item 1 above.
3. At each response period, *T*, greater than 10s, S_a, shall be taken as the value of S_a at the period of 10s of Item 1 above, factored by 10/*T*, where the value of *T* is less than or equal to

that of the long-period transition period, T_L , and shall be taken as the value of S_a at the period of 10s, factored by $10T_L/T^2$, where the value of T is greater than that of the long-period transition period, T_L.

The authors noted that the procedure for the MPRS results in a discontinuity in the response spectrum when T_L is less than 10s; the discontinuity occurs between the S_a at 10s, S_{a10}, and at a period greater than 10s.

The authors recommend that the Item 3 of the Section 11.4.5.1 of ASCE 7-22 be corrected. Currently, Item 3 explains how to calculate the 5%-damped design spectral response acceleration parameter, S_a when the period of interest T is greater than 10s. Item 3 can be summarized using:

$$S_a = \frac{(10)S_{a10}}{T} \tag{2a}$$

when the period of interest T is less than T_L, and S_{a10} is the spectral acceleration at a period of 10s, and:

$$S_a = \frac{(10)T_L S_{a10}}{T^2} \tag{2b}$$

when the period of interest T is greater than T_L. An issue arises when the period of interest is greater than 10s and T_L is less than 10s. Then, immediately after 10s, the S_a would be calculated using Equation 2b. If T_L is less than 10s, the authors propose the following equation for periods of interest greater than 10s:

$$S_a = \frac{(10^2)S_{a10}}{T^2} \tag{2c}$$

Equation 2c ensures continuity. Figure 4 shows the MPRS presented in the 2020 Edition of FEMA 450-1 as the default design response spectrum; Figure 4 shows an example in which T_L is greater than 10s.

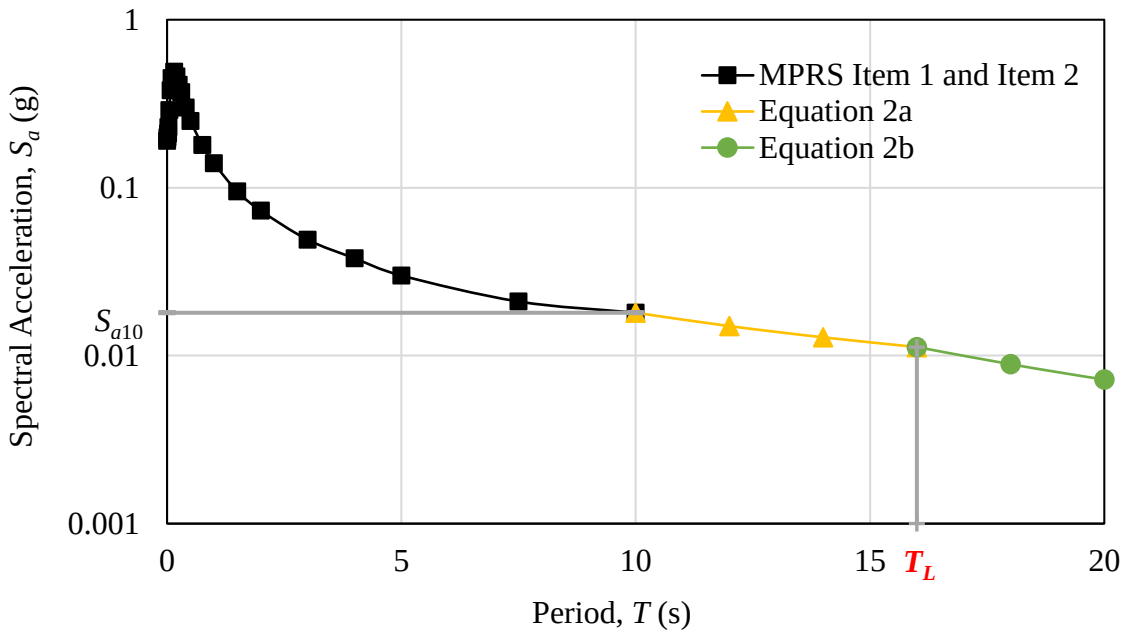

Figure 4. Generic MPRS, First Presented in the 2020 Edition of FEMA 450-1 (BSSC, 2020).

Figure 5 shows an example of a generic MPRS with T_L less than 10s; Figure 5 includes both the current code language Equation 2b and our proposed Equation 2c. The discontinuity using the current code language (Equation 2b) is apparent in Figure 5.

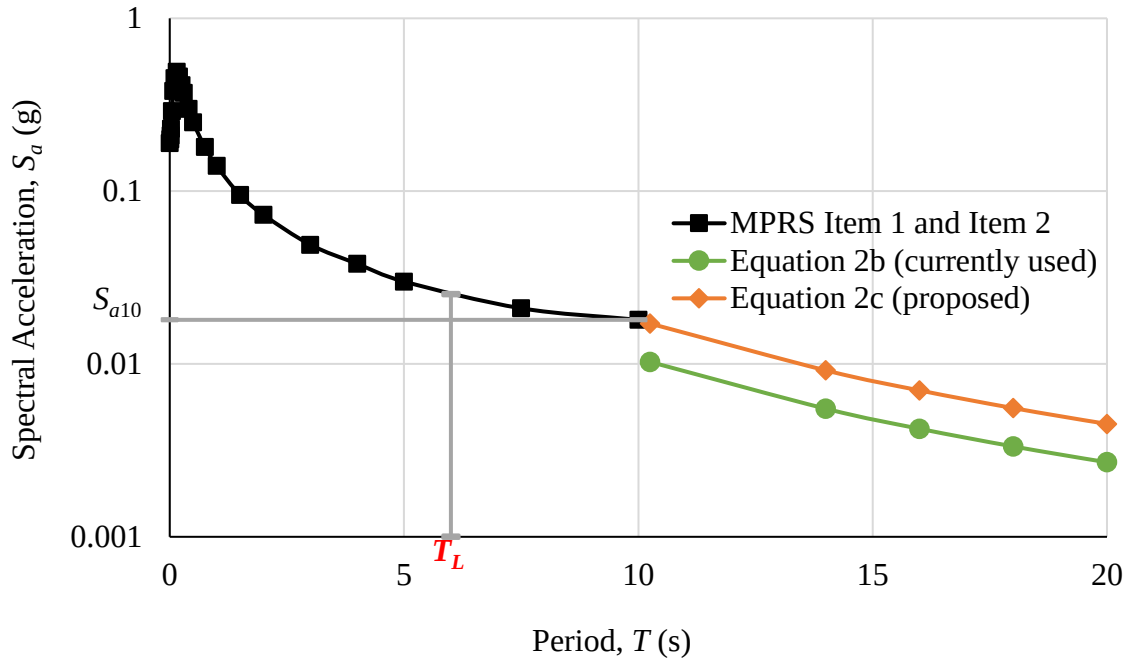

Figure 5. Generic MPRS with T_L less than 10s, and Proposed Equation 2c.

Research Related to T_L and Response Spectra

Although T_L has not been directly investigated in the United States, there has been limited research conducted related to determining T_L in other countries. Fauzi et al. (2011) developed a map of T_L in Indonesia based on the methodology proposed by Crouse et al. (2006) and used in FEMA 450-1 (BSSC, 2004a). According to Crouse et al. (2006), the parameter T_L can be approximated by T_c. However, this is an assumption with no proven basis. McVerry et al. (2017) studied the estimation of T_L in New Zealand based on both Brune-type expressions and analyzing response spectra from recent large New Zealand Earthquakes. McVerry et al. (2017) echoed the need for further investigation into the relationship between T_c and T_L.

In the United States, there has been a wide range of research conducted on the construction of smooth response spectra. Malhotra (2006) developed a method of constructing a smooth response spectrum based on peak ground accelerations, peak ground velocity, and peak ground displacements. Li et al. (2016) built upon the work of Malhotra by considering more ground motions at a variety of soil sites, resulting in the development of site design spectrum coefficients to modify the spectral values of Newmark design spectra in the acceleration sensitive, velocity sensitive, and displacement sensitive regions based on soil site class.

In addition to research related to T_L, research has also been conducted on the disaggregation of seismic hazard into source contributions. Disaggregation of seismic hazard shows the relative contribution of magnitudes and distances contributing to the probability of exceedance of a certain level of hazard. Some sources of literature refer to “deaggregation” instead of “disaggregation,” but both terms refer to the same technique (Bazzurro and Cornell, 1999). Disaggregation techniques have changed over time, as well as disaggregation results from NSHMs (Bazzurro and Cornell, 1999; Harmsen, 2001; Petersen et al., 2019). A

disaggregation of seismic hazard was completed specifically for the construction of T_L maps for FEMA 450-1/2003 (Crouse et al., 2006). Disaggregation was again completed by USGS in 2008, 2014, and 2018 for the CONUS and in 2021 for HI for updates to the NSHM. However, T_L has not been re-computed based on changing disaggregation results over the years.

A Different Approach to Estimating T_L

Our objective for this research is to develop an improved estimation of T_L. Instead of calculating T_L only as a function of M_w as in Equation 1, the definition of corner period will be utilized to estimate T_L as:

$$T_L \approx T_c = \frac{1}{f_c} = \frac{1}{4.9(10^6)\beta}\left(\frac{10^{1.5(10.7+M_w)}}{\Delta\sigma}\right)^{1/3} \quad (3)$$

Equation 3 is the definition of the corner period of the Fourier amplitude spectrum T_c developed by Brune (1970), where the seismic moment M_o is substituted with its definition in terms of M_w developed by Hanks and Kanamori (1979). The corner frequency f_c is the inverse of the corner period, which is also defined as the source duration T_D (Boore, 2003).

There are two primary concerns with using Equation 3: 1) it assumes a single corner frequency (SCF) spectrum and 2) the relationship between T_c and T_L. Both concerns also exist with the original estimation of T_L in Equation 1.

Atkinson and Silva (2000) stated that the primary issue with using an SCF spectrum is that SCF models consistently overpredict ground motions from moderate and large earthquakes at low and intermediate frequencies (0.1–2 Hz), making a SCF model undesirable. However, double-corner frequency (DCF) models have been developed where the lower corner frequency f_{c1} is defined as proportionally the same as the single-corner frequency f_c shown in Equation 3 (Ji and Archuleta, 2021), that is:

$$\frac{1}{f_{c1}} \propto \frac{1}{\beta}\left(\frac{M_o}{\Delta\sigma}\right)^{1/3} \quad (4)$$

So, for the sole purpose of estimating the corner period, a SCF and DCF model yield the same result. Moreover, SCF models are still being developed and used in many ground motion models (GMMs), including the six Boore models presented in the NGA-East project (Goulet et al., 2015). For these reasons, an SCF model was determined to be appropriate for this application.

FEMA 450-1 considers T_c and T_L approximately equal (BSSC, 2004b). T_L is a parameter that is used to represent a specific period when the displacement spectrum is constant of multiple earthquakes that could occur in a geographic location, rather than an actual specific, measurable quantity. McVerry et al. (2017) studied the estimation of T_L in New Zealand based on both Brune-type expressions and analyzing response spectra from five recent large New Zealand Earthquakes. They concluded that for New Zealand the Brune-type seismological expressions were sufficient to estimate T_L for lower magnitude earthquakes, and the analysis of response spectra better-estimated T_L for the larger earthquakes ("larger" meaning earthquakes with $M_w \geq 6$). However, they also stated that further investigation into the relationship between T_c and T_L should be conducted.

Methodology

Following Equation 3, we use regional estimates of M_w, β, and $\Delta\sigma$ to estimate T_L. Estimations of parameters β and $\Delta\sigma$ are split into three broad regions of the United States: The Central and Eastern United States (CEUS) and Western United States (WUS) that comprise the CONUS, and HI. WUS includes all locations in the CONUS west of the boundary used in the 2018 Update of the U.S. NSHM (Petersen et al., 2021). The modal magnitude M_w for a 2% probability of exceedance in 50 years hazard can be determined using the USGS Disaggregation

Web Tool of the 2018 NSHM of the CONUS and the 2021 NSHM of HI (USGS, 2022; Petersen et al., 2019; Petersen et al., 2022). The details of estimating all parameters are described next.

Estimation of β

We use the well-established estimates of source velocity from previous research: β = 3.7 km/s for CEUS, β = 3.5 km/s for WUS, and β = 3.8 km/s for HI (Zandieh et al., 2018; Wong et al., 2021).

Estimation of $\Delta\sigma$

Zandieh et al. (2018) developed estimates for the stress drop in the Western United States (WUS) using an inversion of five ground motion prediction equations (GMPEs) that were developed as part of the PEER NGA-West2 Project (Bozorgnia et al., 2014). The GMPEs used for the inversion are: ASK14 (Abrahamson et al., 2014), BSSA14 (Boore et al., 2014), CB14 (Campbell and Bozorgnia, 2014), CY14 (Chiou and Youngs, 2014), and I14 (Idriss, 2014). We used Zandieh et al.'s (2018) study for WUS sites. Figure 6 shows the estimations of stress drop for the WUS as a function of magnitude.

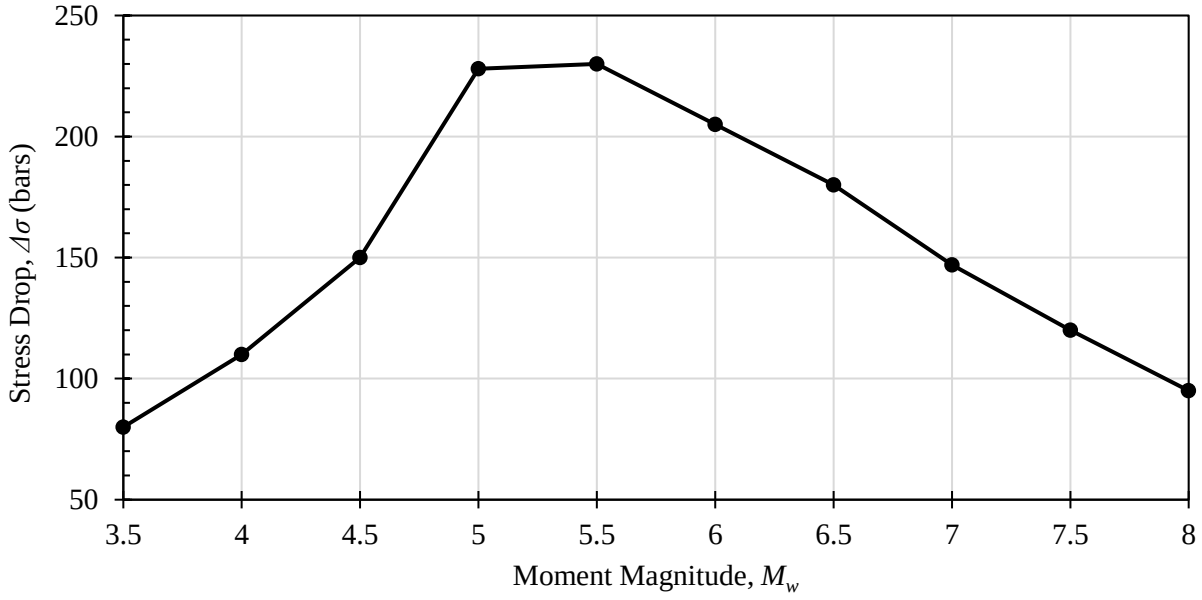

Figure 6. Stress Drop Estimations for WUS (Zandieh et al., 2018).

From Figure 6, the stress drop in WUS ranges from 100 bars to almost 250 bars. A stress drop that rises and then plateaus and/or decreases with magnitude is expected from inversion results (Zandieh et al., 2018).

We used the ground motion models (GMMs) developed for the CEUS (Goulet et al., 2015) to perform an inversion to determine stress drop using an approach similar to that used by Zandieh et al. (2018).

For HI, we used an estimate from Wong et al. (2021) of $\Delta\sigma$ = 20 bars. Wong et al. (2021) performed an inversion of the 2018–2019 Kalapana sequence recorded by the Hawaiian networks and previously recorded crustal events. Then, they developed a crustal earthquake GMM using the stochastic numerical ground motion modeling approach (Silva et al., 1997). They performed an inversion of Fourier amplitude spectra (FAS) for stress drops and other seismological parameters for HI.

Inversion

A methodology similar to that proposed by Zandieh et al. (2018) was used to obtain the stress drop estimations. The following objective function is minimized:

$$Objective\ Function = \sqrt{\sum_{i,j,k} \left(\log(S_{i,j,k}) - \log(G_{i,j,k})\right)^2} \qquad (5)$$

where $S_{i,j,k}$ is the observed spectral acceleration for magnitude i, distance j, and spectral period k, and $G_{i,j,k}$ is the stochastically predicted value of the spectral acceleration from the inversions.

In any inversion problem, there are tradeoffs between parameters. So, each parameter should be constrained within reasonable bounds. The range of each parameter vastly increases or decreases the overall search space for an inversion. A literature review was completed to

determine a reasonable search space for the stress drop parameter. Previous estimations of the stress drop in the CEUS have varied greatly. Goulet et al. (2015) summarize the models used in the development of NGA-East GMMs and cite the mean stress drop from one model as low as 50 bars and another as high as 800 bars. Atkinson (1993) found that CEUS earthquakes have stress drops ranging from 50 to over 400 bars, with a median value of about 150 bars. Boore (2012) determined the stress drop of nine well-recorded earthquakes in the Eastern United States, and the results are also highly varied across the eight earthquakes that the stress drop was estimated for (from 56 bars up to 422 bars). The stress drop was constrained to be between 50 bars and 600 bars for the inversion, since many estimations of stress drop in the CEUS are within that range.

CEUS Ground Motion Models

The GMMs used for the inversion to estimate the stress drop $\Delta\sigma$ in the CEUS were originally developed by Goulet et al. (2015). Then, Goulet et al. (2018) developed standard deviation models and a ground motion characterization (GMC) tool to accompany the GMMs. The final report by Goulet et al. (2018) included 17 GMMs applicable for a range of magnitudes $4 \leq Mw \leq 8.2$ and distances up to 1500 km. A weighted average of the median spectral acceleration of each of the GMMs we used in the inversion were calculated using the GMC tool developed by Goulet et al. (2018). For this study, the inversion was performed for 25 periods ranging from 0.01s to 10s, uniformly distributed in log-space, and for 30 values of R_{RUP} ranging from 1 to 300 km, uniformly distributed in log space. The inversion was performed for individual M_w ranging from 4.0 to 8.0 in 0.5 intervals. The V_{s30} value of 3000 m/s was used, with the site condition adjustment of the NGA-East GMM to the B/C site condition (Vs30 = 760m/s) performed using the site factors in Hashash et al. (2020) and Stewart et al. (2020). Figure 7 shows the estimations for stress drop as a function of moment magnitude.

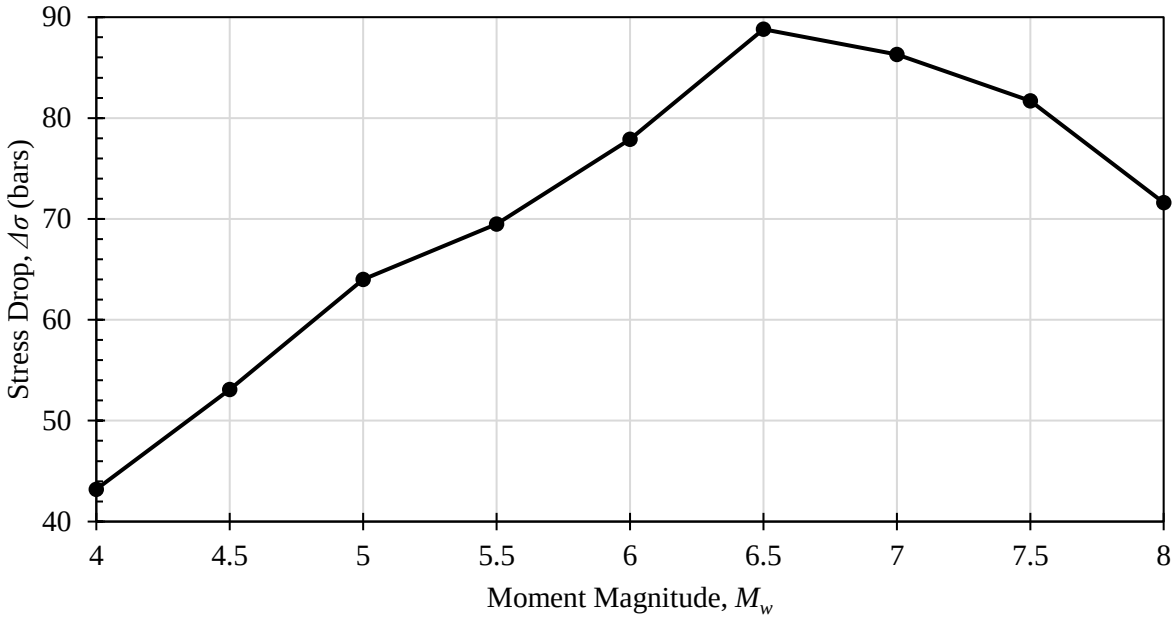

Figure 7. Stress Drop Estimations for CEUS (this study).

As can be observed from Figure 7, the stress drop in the CEUS has a similar trend to that shown in the WUS; however, the stress drop only varies from 40 bars to 90 bars, which is very little. The trend shown in Figure 7 is characteristic of stress drop resulting from an inversion.

Determination of M_w

For the CONUS, we obtained the modal magnitude M_w at grid points with a spacing of 0.5°. The M_w is obtained from the USGS Disaggregation Web Tool using a web driver function of the Selenium module in Python (USGS, 2022). The model used for disaggregation is the NSHM Conterminous U.S. 2018 with a probability of exceedance of 2% in 50 years hazard. In this study, we obtained the modal magnitude M_w disaggregated at a spectral period of 2s and 4s and compared the results. Recall that in the FEMA 450-1 calculation of T_L, 2s was the longest spectral period in which disaggregation could be completed. Now, the USGS Disaggregation

Web Tool can provide disaggregation results for a spectral period up to 10s in some regions and 4s in all regions of the CONUS.

For HI, we developed a grid of points with 0.05° spacing and determined the modal magnitude M_w at each point. The M_w is obtained using the same exact method and tools described for the CONUS. However, the model used for disaggregation is the NSHM Hawaii 2021 and a probability of exceedance of 2% in 50 years hazard (Petersen et al., 2022). For HI, we obtained M_w disaggregated at 1s and 2s and compared the results. Recall that in the FEMA 450-1 calculation of T_L, 1s was the longest spectral period in which disaggregation could be completed for HI. Now, the USGS Disaggregation Web Tool can provide disaggregation results for a spectral period up to 10s in HI.

The hazard level will not change from the disaggregation originally determined to develop T_L maps in FEMA 450-1 and in this study, because the probability of exceedance is the same. A probability of exceedance of 2% in 50 years is used in determining the spectral acceleration for the design response spectrum, so we used the same hazard level for the determining M_w in this study.

Comparison of M_w at Different Spectral Periods

When T_L was first developed, a spectral period of 2s (for the CONUS) and 1s (for HI) were considered sufficiently long spectral periods to calculate T_L (Crouse et al., 2006). However, in some areas, the modal magnitude at a spectral period of 1s or 2s can be very different than the modal magnitude at longer spectral periods. So, a sensitivity analysis was conducted. Figure 8a shows a map of the numerical difference between the modal magnitude at 4s, $M_{w(4s)}$ and modal magnitude 2s, $M_{w(2s)}$ with all other parameters the same. The spectral period of 4s was chosen to compare to 2s, because 4s is the longest spectral period available at every

site in the CONUS. From the estimations of modal magnitude at both spectral periods, we were able to estimate T_L using these different modal magnitudes and compare them. Figure 8b shows the numerical difference between T_L estimated using Equation 3, with the modal magnitude at a spectral period of 4s, $T_{L(4s)}$ and T_L estimated from the modal magnitude at a spectral period of 2s, $T_{L(2s)}$.

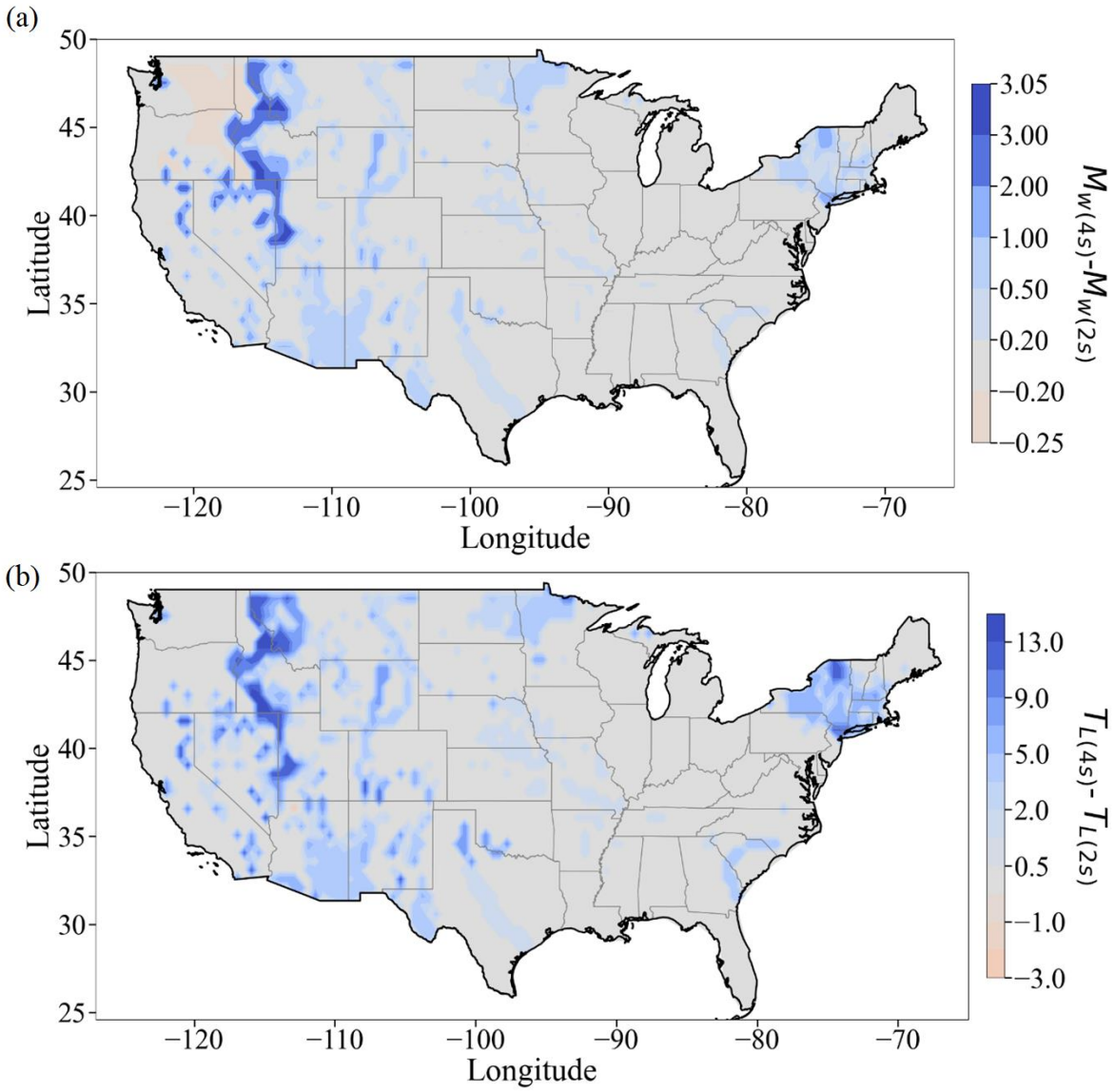

Figure 8. (a) Difference in Modal Magnitude at Spectral Period of 4s, $M_{w(4s)}$ and Modal Magnitude at Spectral Period of 2s, $M_{w(2s)}$ and (b) Difference in T_L Using Equation 3 with the Modal Magnitude at a Spectral Period of 4s, $T_{L(4s)}$ and T_L Using the Modal Magnitude at a Spectral Period of 2s, $T_{L(2s)}$.

As can be observed from Figure 8a, the difference between the modal magnitude at spectral periods of 4s and 2s is less than 1.0 for all the CEUS. However, in the WUS, many areas have a difference of 2, and for a significant area there is a difference of over 3. As can be observed from Figure 8b, again, there is very little variation in the CEUS (except for the New York area), and high variation in the WUS. In the WUS, there is a difference over 5 seconds in many areas and over 13.5 seconds difference in a significant area. Further analysis of the correlation between the spectral period and modal magnitude needs to be conducted.

After analyzing Figure 8, we decided to use a spectral period of 2s for several reasons. First, the estimated T_L from this study at a spectral period of 2s is already longer (or more conservative) compared to the T_L from FEMA 450-1. Figure 9 shows the mapped modal magnitude at a spectral period of 2s, used in the calculation of T_L for the CONUS.

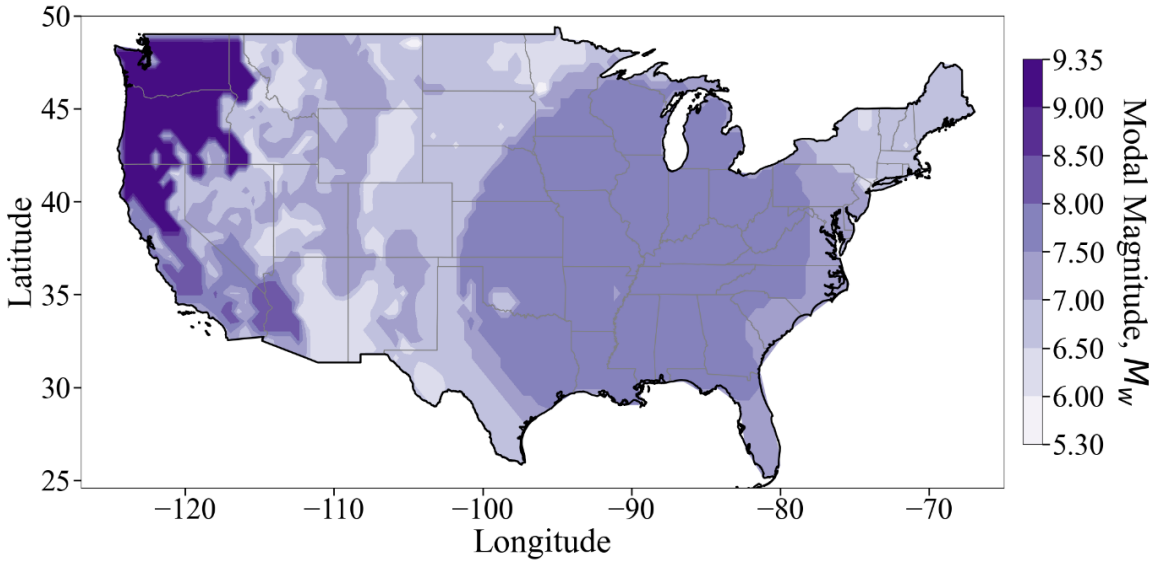

Figure 9. Mapped Modal Magnitude at a spectral period of 2s in the CONUS.

As can be observed from Figure 9, the modal magnitude at a spectral period of 2s ranges from 5.3 to 9.35 in the CONUS. M_w is the largest in the northwest corner of the CONUS and is between 7.5 and 8 in a majority of the CEUS. It should be noted that the M_w disaggregated at a spectral period of 2s shown in Figure 9 is still different than the M_w disaggregated for the original development of M_w and T_L maps, since disaggregation has been re-done several times by USGS through the NSHM (Crouse et al., 2006; Petersen et al., 2019).

When T_L was originally developed for HI, M_w was disaggregated at a spectral period of 1s. Figure 10 shows a map of a) the numerical difference between the modal magnitude at 2s, $M_{w(2s)}$ and modal magnitude at 1s, $M_{w(1s)}$ with all other parameters kept the same for HI and b) the numerical difference between the modal magnitude at 4s, $M_{w(4s)}$ and modal magnitude 1s, $M_{w(1s)}$ with all other parameters kept the same for HI.

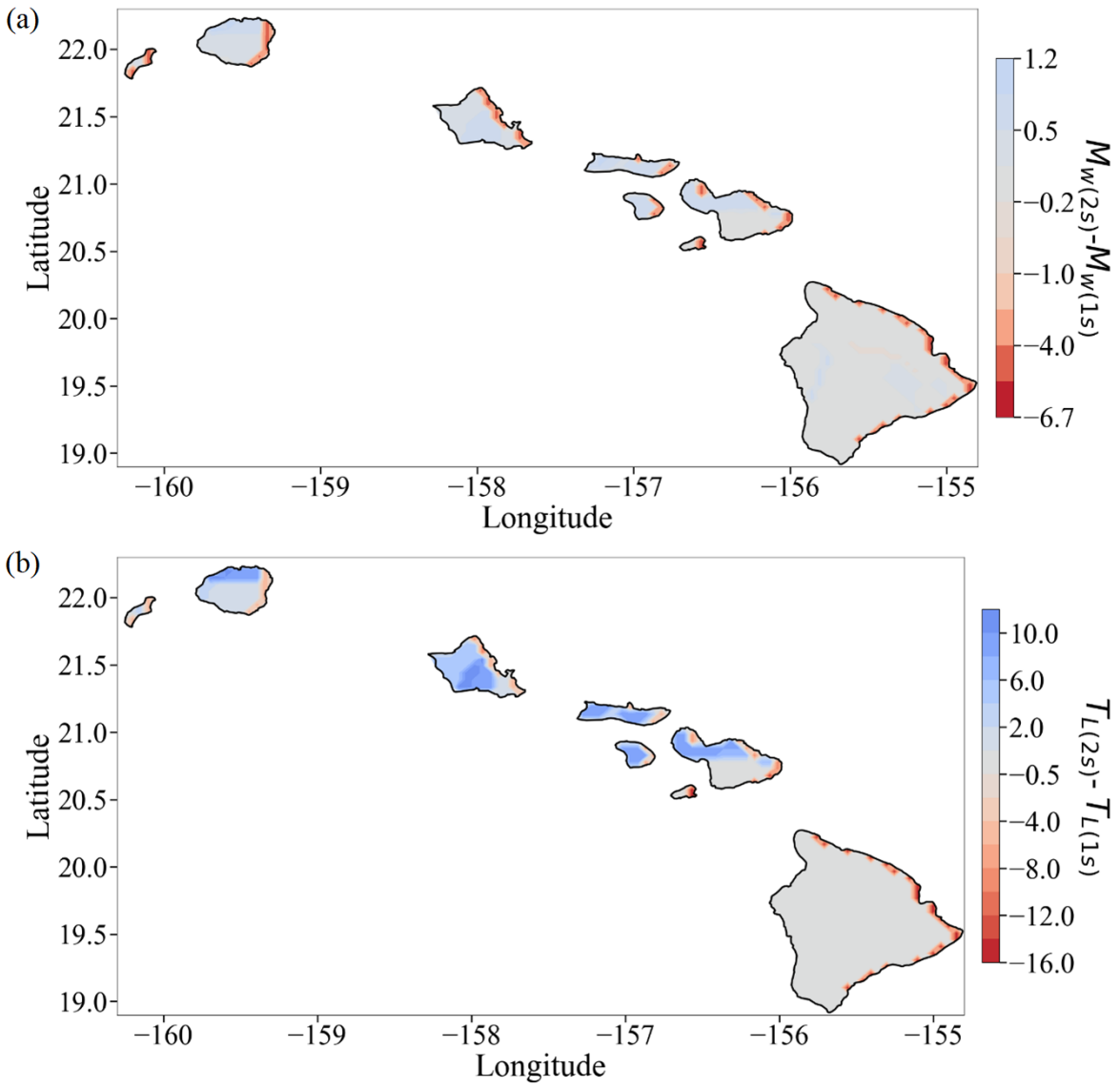

Figure 10. (a) Difference in Modal Magnitude at Spectral Period of 2s, $M_{w(2s)}$ and Modal Magnitude at Spectral Period of 1s, $M_{w(1s)}$ for HI and (b) Difference in T_L Using the Modal Magnitude at a Spectral Period of 2s, $T_{L(2s)}$ and T_L Using the Modal Magnitude at a Spectral Period of 1s, $T_{L(1s)}$ for HI.

As can be observed from Figure 10a, $M_{w(1s)}$ is much larger than $M_{w(2s)}$ along many of the borders of the islands by as much as 6.7 but are in closer agreement elsewhere. Figure 10a shows conflicting results, as there is not a direct correlation between the spectral period and M_w; a longer spectral period does not always result in a larger M_w. As can be observed from Figure

10b, in some areas, $T_{L(2s)}$ is more than $T_{L(1s)}$ by more than 10 seconds, and in other areas $T_{L(2s)}$ is almost 16 seconds less than $T_{L(1s)}$.

After analyzing Figure 10, we recommend using a spectral period of 1s for HI. The estimated T_L from this study at a spectral period of 1s is already longer (or more conservative) compared to the simplification of T_L from FEMA 450-1. The differences shown in Figure 10 show a need for further investigation regarding the effect of the spectral period on T_L in HI in future studies. Figure 11 shows the mapped modal magnitude at a spectral period of 1s, used in the calculation of T_L for HI.

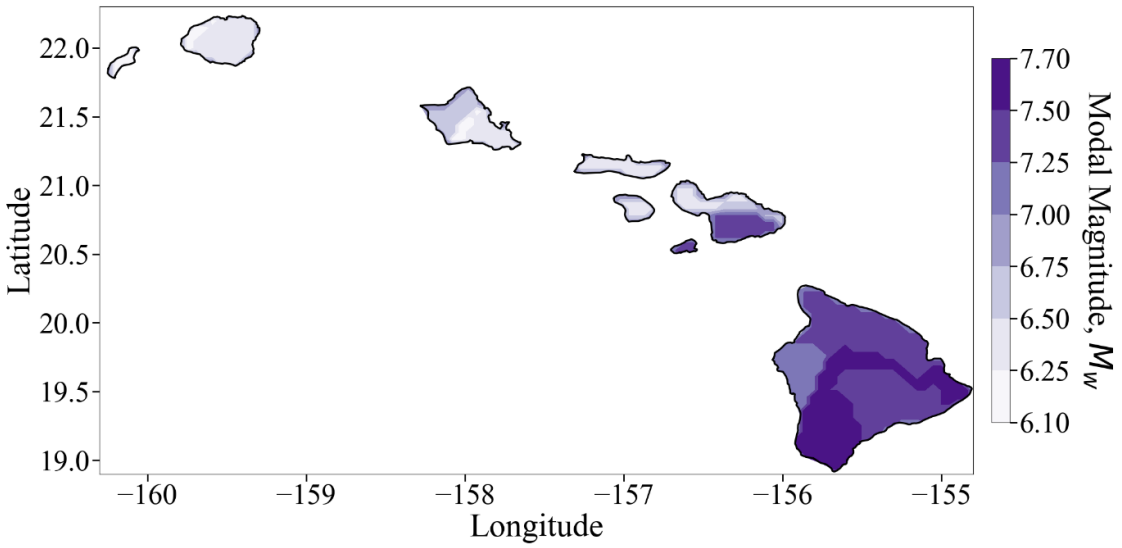

Figure 11. Modal Magnitude at a spectral period of 1s in HI.

In Figure 11, the modal magnitude ranges from 6.1 to 7.7 in HI. It should be noted that the M_w disaggregated at a spectral period of 1s shown in Figure 11 is still different than the M_w disaggregated for the original development of M_w and T_L maps for HI, since disaggregation has been re-done in HI by USGS through the NSHM (Crouse et al., 2006; Petersen et al., 2022).

The current limit for T_L is 16 seconds in the WUS and Alaska, citing the analysis of response spectra from simulated ground motions from models of large subduction-zone earthquakes (Crouse et al., 2006; Gregor et al., 2002). However, the response spectra from

Gregor et al. (2002) were only developed for a period up to 5 seconds, making it unclear how that conclusion was made. T_L is currently limited to 12 seconds in the CEUS, without justification (Crouse et al., 2006). The authors agree that 16 seconds is a reasonable limit nationally, given that hardly any structures have a fundamental period that high.

Results

Once stress drop was determined as a function of moment magnitude in the WUS and CEUS, and the appropriate modal magnitude was selected, stress drop was mapped corresponding to the estimated modal magnitude at each site. Figure 12 shows the mapped stress drop from the magnitude-dependent estimates from Zandieh et al. (2018) for WUS and the inversion of the GMMs for CEUS completed for this study.

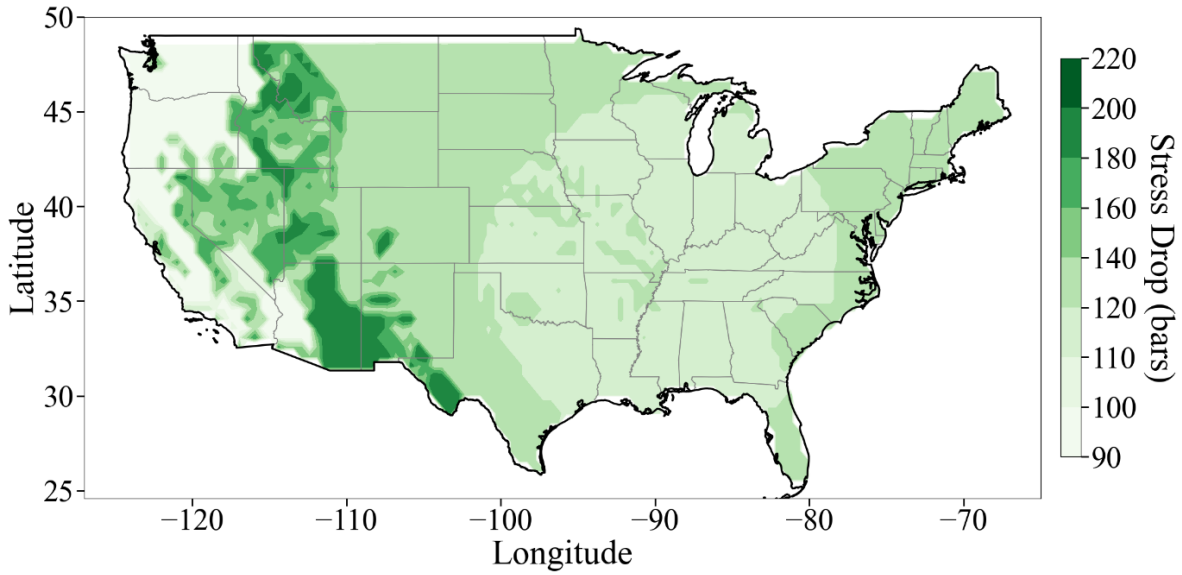

Figure 12. Stress Drop (bars) in the CONUS.

From the regional estimates of stress drop and source velocity, Equation 3 was used to estimate T_L for this study. Figure 13 compares T_L as a function of M_w when using Equation 1, the ASCE 7 simplification of Equation 1, and Equation 3 for the three broad regions of the United States mentioned in this study: CEUS, WUS, and HI.

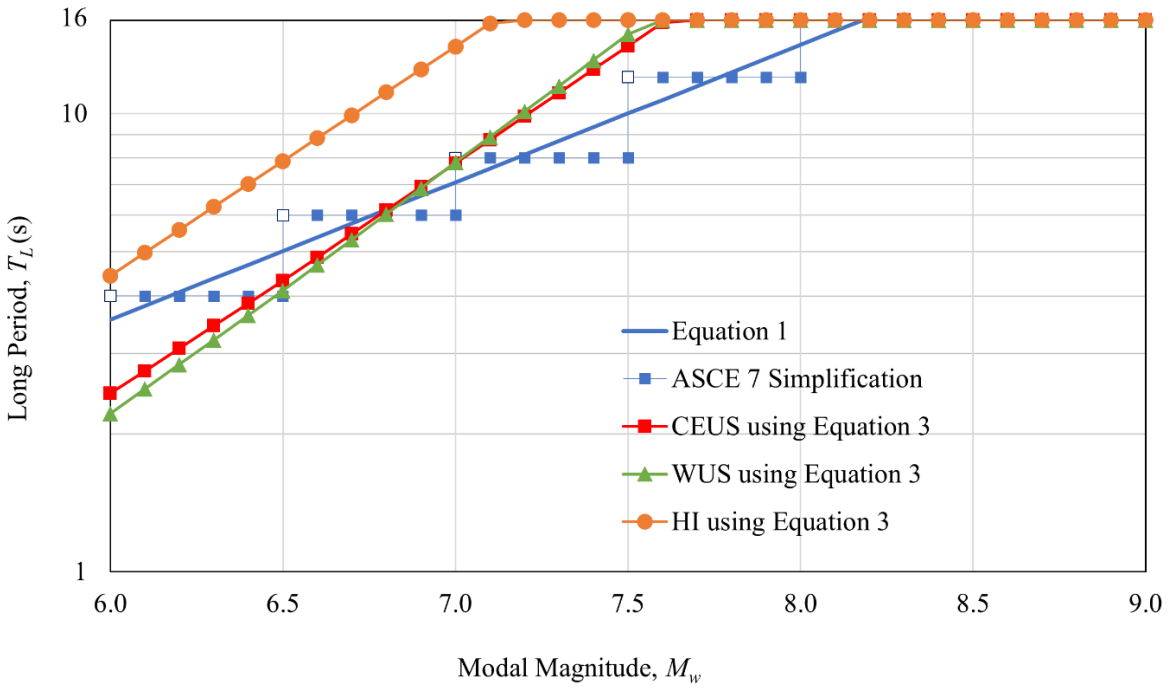

Figure 13. Comparison of T_L Used Currently (Equation 1; ASCE 7 Simplification), and Estimations Proposed in This Study (CEUS using Equation 3; WUS using Equation 3; HI using Equation 3).

From Figure 13, FEMA 450-1 has lower values of T_L in the CEUS and WUS for a M_w greater than 6.7., whereas FEMA 450-1 has lower values of T_L in HI for M_w greater than 6. The CEUS, WUS, and HI models all estimate a steeper slope for T_L vs. M_w than Equation 1 or its simplification. Figure 13 also demonstrates a more customized approach to determining T_L using the methodology in this study; rather than having one line that estimates T_L for the entire United States, this study has three unique lines that estimate T_L in the CEUS, WUS, and HI separately. The slope of the line in Figure 13 is primarily affected by β, whereas the shifting of the line upwards and downwards is primarily affected by the estimate of $\Delta\sigma$.

Figure 14 shows estimates of T_L in the CONUS from this study. Figure 15 shows the estimates of T_L in HI from this study. The authors recommend that 16 seconds is a sufficiently long period to limit T_L nationally, considering that very few structures will have a structural period that long, and that limit is reflected in Figure 14 and Figure 15.

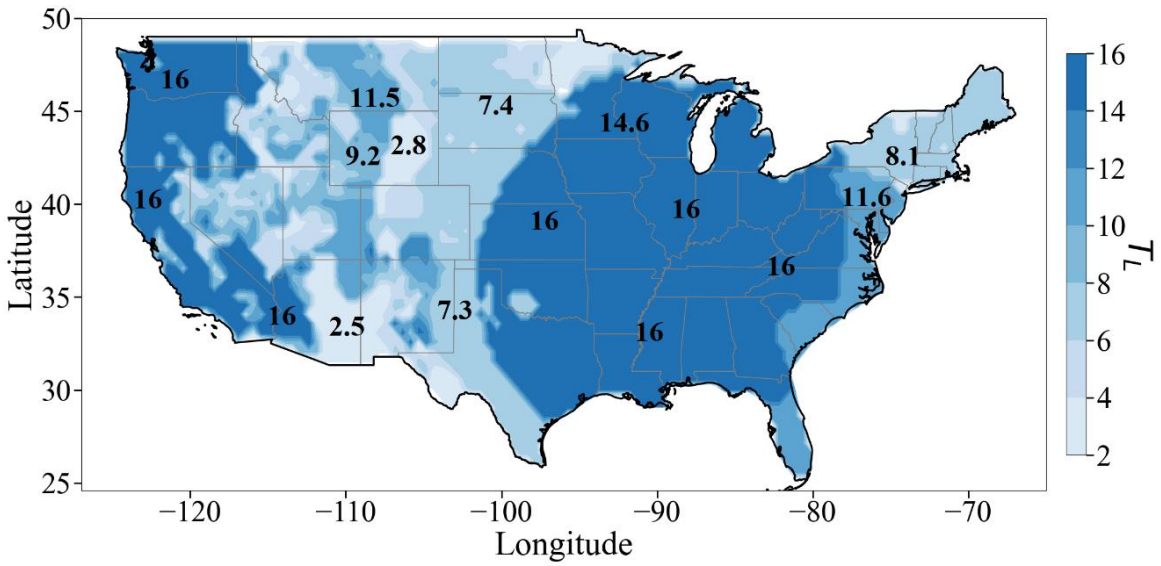

Figure 14. Estimates of T_L using Equation 3 in the CONUS. The Bold Numbers in Each Region Represent T_L for that Region.

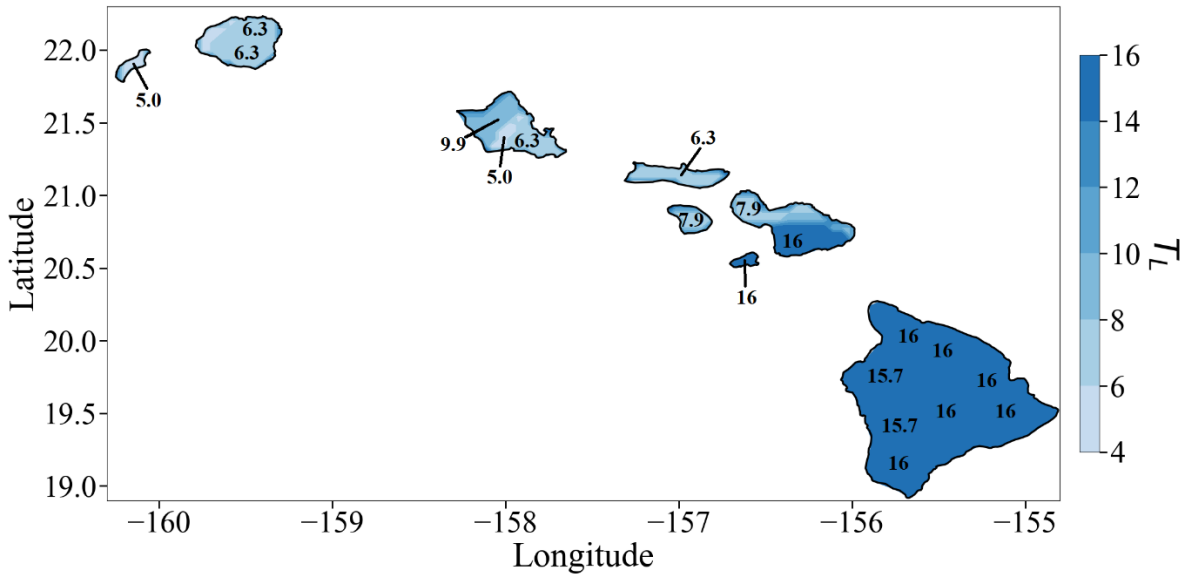

Figure 15. Estimates of T_L using Equation 3 in HI. The Bold Numbers in Each Region Represent T_L for that Region.

This study's estimates of T_L in Figure 14 and Figure 15 were subtracted from the ASCE 7 simplification of Equation 1, $T_{L(NEHRP)sim}$, to determine the difference (in seconds) between the two at each site. Figure 16 shows the numerical difference between the simplification of FEMA

450-1's Equation 1, $T_{L(NEHRP)sim}$ and T_L estimated from this study in the CONUS. Figure 17 shows the same numerical difference for HI.

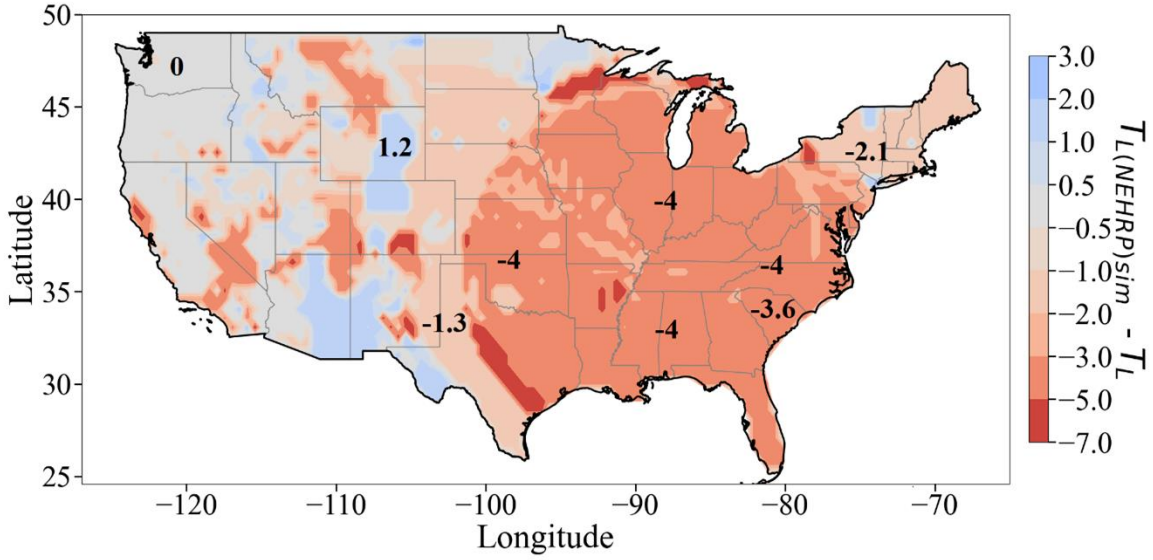

Figure 16. Difference between the ASCE 7 simplification of Equation 1, $T_{L(NEHRP)sim}$ and this study's estimation of T_L in the CONUS. The areas that are positive are where the $T_{L(NEHRP)sim}$ is longer than T_L computed in this study, and the areas that are negative are where $T_{L(NEHRP)sim}$ is shorter than T_L computed in this study.

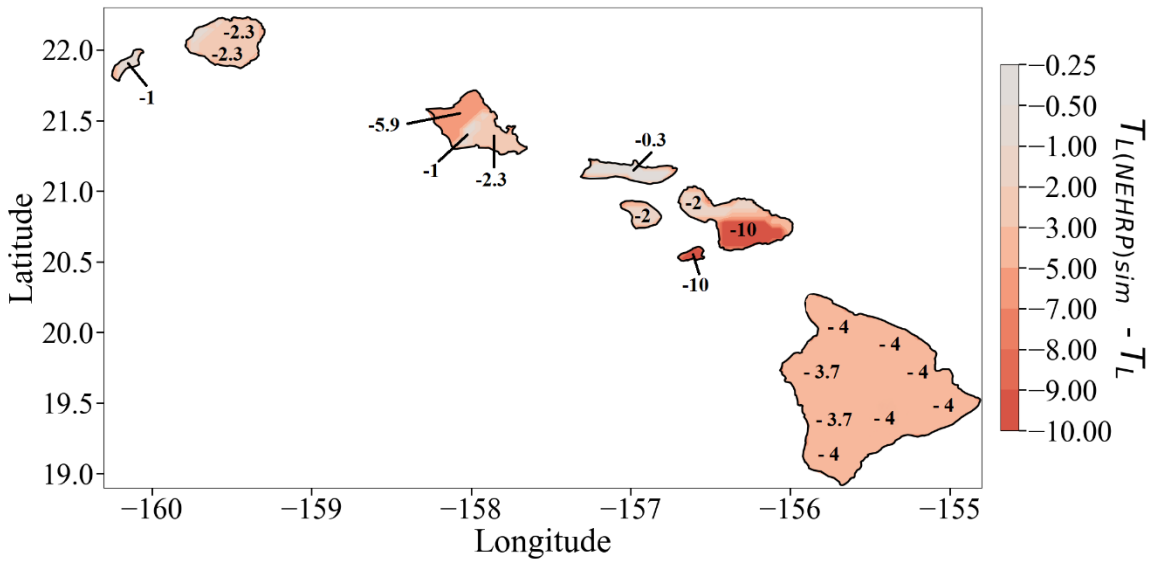

Figure 17. Difference between the ASCE 7 simplification of Equation 1, $T_{L(NEHRP)sim}$ and this study's estimation of T_L in HI. Since all areas of this map are negative, that means that $T_{L(NEHRP)sim}$ is shorter than T_L computed in this study at every location in HI.

Figure 16 and Figure 17 show a significant discrepancy in $T_{L(NEHRP)sim}$ and T_L computed in this study for many regions of the United States. These differences are expected considering that M_w is greater than 5.3 in all locations in the United States and the formulations for T_L developed in this study are longer than $T_{L(NEHRP)sim}$ for $M_w > 6.7$.

It is important to note again that the numerical difference shown in Figure 16 and Figure 17 is between the $T_{L(NEHRP)sim}$ (shown in Figure 1) and Equation 3, not between $T_{L(NEHRP)}$ and Equation 3. The reason why is that it demonstrates the actual change in seconds that T_L could differ in the building codes in the future.

Conclusions

The results of this study are generally more conservative than the estimation of T_L currently used in FEMA 450-1. There are numerous regions where FEMA 450-1's estimation is more conservative, however it is longer by at most 3 seconds in those regions, whereas our

estimation is longer than FEMA 450-1's estimation by up to 7 seconds in the CONUS and 10 seconds in HI.

When T_L was first introduced in Crouse et al. (2006) as a new parameter, it was noted that T_L would likely need to be investigated and refined. However, since its inception, T_L has not been modified. This study aimed to address concerns raised over the estimation of T_L. One concern with the current estimation of T_L is using one equation (ASCE 7 simplification of Equation 1; $T_{L(NEHRP)sim}$) for the entire country, despite differences in seismological parameters. With regional estimations of seismological parameters available, T_L can be calculated anywhere with estimations of $\Delta\sigma$ and β. A concern that was specifically expressed in the introduction of T_L in Crouse et al. (2006) is the harsh borders between areas of a high T_L to an area with a lower T_L. This study estimates T_L on a 0.5° spacing in the CONUS and a 0.05° spacing in HI, resulting in a high-resolution contour map with thin bands between very high values and lower values of T_L. Furthermore, any site within the CONUS is within 17.25 miles of an estimation of T_L, and any site in HI is within 1.725 miles. The last concern raised over the current estimation of T_L is that it has not been updated along with new disaggregation data that has resulted in new estimations of modal magnitude. This study used the most recent disaggregation data available from the 2018 NSHM of the CONUS and 2021 NSHM of HI (Petersen et al., 2019; Petersen et al., 2022).

There are several limitations to the methodology used in this study. Firstly, the relationship between the spectral period that the modal magnitude is being determined and T_L is unknown and has not been investigated. With no recorded ground motions of $M_w \geq 6.5$ available but a known history of large-magnitude earthquakes in the New Madrid seismic zone (NMSZ), the expressions developed by Brune (1970) were used for even large-magnitude earthquakes. An alternative methodology for determining T_L that could be investigated in future studies is

estimating T_L using displacement response spectra developed from NGA-West2 GMPEs or from NGA-East GMMs. Additionally, T_L was only calculated for the CONUS and Hawaii. Once disaggregation data and estimates of seismological parameters are readily available in Alaska and US territories, T_L needs to be investigated and potentially modified in those areas as well.

Data and Resources

The ground motion characterization (GMC) tool for the CEUS GMMs is available at https://www.risksciences.ucla.edu/nhr3/ngaeast-gmtools from Goulet et al. (2018). The USGS Disaggregation Web Tool is available at https://earthquake.usgs.gov/nshmp/ from USGS (2022). The longitude coordinates, latitude coordinates, and final T_L values calculated in this study are available at https://github.com/cmmore11/TL_US_Estimation_2022.

References

Abrahamson, N. A., Silva, W. J., and Kamai, R., 2014. Summary of the ASK14 ground motion relation for active crustal regions, *Earthquake Spectra* **30**, 1025–1055.

American Society of Civil Engineers (ASCE), 2005. *Minimum Design Loads for Buildings and Other Structures, ASCE/SEI 7–05*, Reston, VA.

American Society of Civil Engineers (ASCE), 2016. *Minimum Design Loads for Buildings and Other Structures, ASCE/SEI 7–16*, Reston, VA.

American Society of Civil Engineers (ASCE), 2022. *Minimum Design Loads for Buildings and Other Structures, ASCE/SEI 7–22*, Reston, VA.

Atkinson, G. M., 1993. Earthquake Source Spectra in Eastern North America, *Bulletin of the Seismological Society of America* **83(6)**, 1778–1798.

Atkinson, G. M., and Silva, W. J., 2000. Stochastic modeling of California ground motions, *Bulletin of the Seismological Society of America* **90(2)**, 255–274.

Bazzurro, P., and Cornell, C. A., 1999. Disaggregation of Seismic Hazard, *Bulletin of the Seismological Society of America* **89(2)**, 501-520.

Bommer, J. J., Elnashai, A. S., and Weir, A. G., 2000. Compatible Acceleration and Displacement Spectra for Seismic Design Codes, in *Proceedings, 12th World Conference on Earthquake Engineering*, 30–4 January/February, 2000, Upper Hutt, New Zealand.

Boore, D. M., 2003. Prediction of ground motion using the stochastic method, *Pure Applied Geophysics* **160**, 635–676.

Boore, D. M., 2012. Updated Determination of Stress Parameters for Nine Well-Recorded Earthquakes in Eastern North America, *Seismological Research Letters* **83(1)**, 190–-199.

Boore, D. M., Stewart, J. P., Seyhan, E. and Atkinson, G. M., 2014. NGA-West2 equations for predicting PGA, PGV, and 5% damped PSA for shallow crustal earthquakes, *Earthquake Spectra* **30**, 1057–1085.

Bozorgnia, Y., Abrahamson, N. A., Atik, L. A., Ancheta, T. D., Atkinson, G. M., Baker, J. W., Baltay, A., Boore, D. M., Campbell, K. W., Chiou, B. S. J., et al., 2014. NGA-West2 research project, *Earthquake Spectra* **30**, 973–987.

Building Seismic Safety Council (BSSC), 2004a. *NEHRP Recommended Provisions for Seismic Regulations for New Buildings and Other Structures Provisions*, Washington, DC.

Building Seismic Safety Council (BSSC), 2004b. *NEHRP Recommended Provisions for Seismic Regulations for New Buildings and Other Structures Commentary*, Washington, DC.

Building Seismic Safety Council (BSSC), 2015. *NEHRP Recommended Provisions for Seismic Regulations for New Buildings and Other Structures Provisions and Commentary*, Washington, DC.

Building Seismic Safety Council (BSSC), 2020. *NEHRP Recommended Provisions for Seismic Regulations for New Buildings and Other Structures Provisions and Commentary*, Washington, DC.

Brune, J. N., 1970. Tectonic Stress and the Spectra of Seismic Shear Waves from Earthquakes, *Journal of Geophysics Research* **75(26)**, 4997–5009.

Campbell, K. W., and Bozorgnia, Y., 2014. NGA-West2 ground motion model for the average horizontal components of PGA, PGV, and 5% damped linear acceleration response spectra, *Earthquake Spectra* **30**, 1087–1115.

Chiou, B. S.-J., and Youngs, R. R., 2014. Update of the Chiou and Youngs NGA model for the average horizontal component of peak ground motion and response spectra, *Earthquake Spectra* **30**, 1117–1153.

Idriss, I. M., 2014. An NGA-West2 empirical model for estimating the horizontal spectral values generated by shallow crustal earthquakes, *Earthquake Spectra* **30**, 1155–1177.

Crouse, C. B., Leyendecker, E. V., Somerville, P. G., Power, M., and Silva, W. J., 2006. Development of Seismic Ground-motion Criteria for The ASCE 7 Standard, in *Proceedings, 8th US National Conference on Earthquake Engineering 2006*, 18–22 April, 2006, Oakland, California.

Fauzi, U. J., Fauzi, A., Irsyam, M., Toha, F. X., and Hendriyawan, H., 2011. Proposed Long-Period Transition Map for New Indonesia Earthquake Resistant Building Code based on Indonesia Seismic Hazard Map 2010, in *Proceedings, Annual International Conference Syiah Kuala University 2011*, 29–30 November, 2011, Banda Aceh, Indonesia.

Goldberg, D. E., 1989. *Genetic algorithms in search, optimization, and machine learning.* Addison-Wesley Publishing Company, Inc., New York, NY.

Goulet, C. A., Bozorgnia, Y., and Abrahamson, N. A., 2015. *PEER NGA-East: Median Ground Motion Models for the Central and Eastern North America Region, Tech. Rep. Pacific Earthquake Engineering Research Center (PEER) 2015/04*. Berkeley, California.

Goulet, C. A., Bozorgnia, Y., Abrahamson, N. A., Kuehn, N., Atik, L. A., Youngs, R., and Graves, R., 2018. *Central and Eastern North America Ground-Motion Characterization - NGA-East Final Report, Tech. Rep. Pacific Earthquake Engineering Research Center (PEER) 2018/08*. Berkeley, California.

Goulet, C. A., Bozorgnia, Y., Abrahamson, N. A., Kuehn, N., Atik, L. A., Youngs, R., and Graves, R., 2018. *NGA-East Ground Motion Characterization Tool (GMC)*, software, https://www.risksciences.ucla.edu/nhr3/ngaeast-gmtools.

Gregor, N. J., Silva, W. J., Wong, I. G., and Youngs, R., 2002. Ground Motion Attenuation Relationship for Cascadia Subduction Zone Megathrust Earthquakes Based on a Stochastic Finite Fault Model, *Bulletin of the Seismological Society of America* **92(5)**, 1923–1932.

Hanks, T. C., and Kanamori, H., 1979. A Moment Magnitude Scale, *Journal of Geophysical Research* **84(5)**, 2348–2350.

Hashash, Y. M. A., Okan, I., Harmon, J. A., Parker, G. A., Stewart, J. P., Rathje, E. M., Campbell, K. C., and Silva, W. J., 2020. Nonlinear site amplification model for ergodic seismic hazard analysis in Central and Eastern North America, *Earthquake Spectra* **36(1)**, 69–86.

Ji, C., and Archuleta, R. J., 2021. A source physics interpretation of non-self-similar double-corner frequency source spectral model JA19_2S, *Bulletin of the Seismological Society of America* **111(2)**, 737–761.

Kircher & Associates, 2015. *Investigation of an identified shortcoming in the seismic design procedures of ASCE 7-10 and development of recommended improvements for ASCE 7-16*, Washington, DC.

Kircher, C. A., Rezaeian, S., and Luco, N., 2019. Proposed Multi-Period Response Spectra and Ground Motion Requirements of the 2020 NEHRP Recommended Provisions and ASCE 7-22, in *Proceedings, 2019 SEAOC Convention*, 28-31 August, 2019, Squaw Creek, California.

Harmsen, S., 2001. Mean and modal epsilon in the deaggregation of probabilistic ground motion, *Bulletin of the Seismological Society of America* **91**, 1537-1552.

Koza, J. R., 1992. *Genetic programming: on the programming of computers by means of natural selection,* Massachusetts Institute of Technology Press, Cambridge, MA.

Li, B., Xie, W. C., and Pandey, M. D., 2016. Newmark design spectra considering earthquake magnitudes and site categories, *Earthquake Engineering and Engineering Vibration* **15(1)**, 519–535.

Malhotra, P. K., 2006. Smooth Spectra of Horizontal and Vertical Ground Motions, *Bulletin of the Seismological Society of America* **96(2)**, 506–518.

McVerry, G. H., Houtte, C. V., Kaiser, A., Holden, C., Fry, B., and Gerstenberger, M., 2017. The Transition Period T_L in the Recommended Spectra of The Draft *New Zealand Seismic Isolation Guidelines*, in *Proceedings, 2017 New Zealand Society for Earthquake Engineering Conference*, 27–29 April, 2017, Wellington, New Zealand.

Menke, W., 2018. *Geophysical Data Analysis: Discrete Inverse Theory*, 4th edition, Academic Press, London, England.

Newmark, N. M., and Hall, W. J., 1973. *Procedures and criteria for earthquake-resistant design, Building practices for disaster mitigation*, U. S. Department of Commerce **Building sciences series 46**, Washington, DC.

Petersen, M. D., Shumway, A. M., Powers, P. M., Mueller, C. S., Moschetti, M. P., Frankel, A. D., Rezaeian, S., McNamara, D. E., Luco, N., Boyd, O. S., Rukstales, K. S., Jaiswal, K. S., Thompson, E. M., Hoover, S. M., Clayton, B. S., Field, E. H., and Zeng, Y., 2019. 2018 Update of the U.S. National Seismic Hazard Model: Overview of Model and Implications, *Earthquake Spectra* **36(1)**, 5–41.

Petersen, M. D., Shumway, A. M., Powers, P. M., Moschetti, M. P., Llenos, A. L., Michael, A. J., Mueller, C. S., Frankel, A. D., Rezaeian, S., Rukstales, K. S., McNamara, D. E., Okubo, P., Zeng, Y., Jaiswal, K. S., Ahdi, S. K., Altekruse, J. M., Shiro, B., 2022. 2021 U.S. National Seismic Hazard Model (NSHM) for the State of Hawaii, *Earthquake Spectra* **38**, 865–916.

Silva, W. J., Abrahamson, N. A., Toro, G., and Constantino, C., 1997. Description and validation of the stochastic ground motion model. Unpublished report prepared for the Brookhaven National Laboratory. Brookhaven National Laboratory, Upton, NY.

Stewart, J. P., Parker, G. A., Atkinson, G. M., Boore, D. M., Hashash, Y. M. A., and Silva, W. J., 2020. Ergodic site amplification model for central and eastern North America, *Earthquake Spectra* **36(1)**, 42–68.

United States Geological Survey (USGS), 2022. *beta: NSHM Hazard Tool*, software, https://earthquake.usgs.gov/nshmp/.

United States Nuclear Regulatory Committee (USNRC), 1973. *Regulatory Guide 1.60, Design Response Spectra for Seismic Design of Nuclear Power Plants*, Washington, DC.

Wong, I., Darragh, R., Smith, S., Wu, Q., Silva, W. J., Kishida, T., 2021. Ground motion models for shallow crustal and deep earthquakes in Hawaii and analyses of the 2018 M 6.9 Kalapena sequence, *Earthquake Spectra* **38(1)**, 579-614.

Zandieh, A., Pezeshk, S., and Campbell, K. W., 2018. An equivalent point-source stochastic simulation of the NGA-West2 ground-motion prediction equations, *Bulletin of the Seismological Society of America* **108(2)**, 815–835.

Chapter 4: Conclusions

The work of this dissertation was carried out in two related studies, where I was responsible for the literature review, creating MATLAB or Python codes or modifying existing MATLAB or Python codes to solve different parts of the problems and develop resulting figures, and writing the bulk of the methodology, results, and conclusions. The other authors thought of the initial ideas, guided the direction of the projects, and provided thorough feedback on the work that I developed.

In the first study, seismological parameters were determined from inverting the median PSA from the NGA-East GMMs. The PSA predicted from the resulting stochastic model agrees well with the median of the NGA-East GMMs, well within the total, or ergodic, standard deviation at each data point. The main limitation of this study is the non-uniqueness of the resulting parameters.

The resulting seismological parameters inform ground motion modelers about the CEUS and are useful for several future works. One way these parameters can be utilized is in developing a stochastic point-source model using even fewer parameters by fitting curves through the existing results as a function of magnitude and frequency. Another future application of the results would be employing the HEM.

The second study investigated the current methodology used to calculate the long period transition period parameter, T_L. The long period transition period parameter is utilized to some degree in both the two-period design response spectrum and the MPRS. In general, the resulting T_L from this study is longer than the T_L currently used.

Future work regarding this second study could include (1) considering measured stress parameters from various earthquakes, (2) comparing results from this study with results from

response spectra from various earthquakes, or (3) smoothing of boundaries between areas where there is a sharp increase or decrease in T_L.